ACS Catalysis

pubs.acs.org/acscatalysis

Research Article

Brønsted Acid Strength Does Not Change for Bulk and External Sites of MFI Except for Al Substitution Where Silanol Groups Form

Haliey Balcom,[§] Alexander J. Hoffman,[§] Huston Locht, and David Hibbitts*

Cite This: *ACS Catal.* 2023, 13, 4470−4487

Read Online

ACCESS | Metrics & More | Article Recommendations | Supporting Information

ABSTRACT: Zeolite synthesis efforts have recently focused on tuning diffusion path lengths by modifying the crystal habit, incorporating mesopores, and using pillared and finned materials to decrease diffusion path lengths, increase rates, and limit zeolite deactivation. These modifications also increase the surface-area-to-volume ratio, increasing the relevance of external Brønsted acid sites. The behaviors of such sites, however, are difficult to study by conventional kinetic studies. Here, we study the acid strength of sites that form on the surfaces of MFI zeolites using density functional theory and compare them to sites within the crystal. We determine acid strength by calculating heterolytic and homolytic O−H bond cleavage energies [deprotonation energy (DPE) and dehydrogenation energy (DHE), respectively] and the adsorption energy of ammonia (ΔE_{NH_3}), a common base titrant. These metrics indicate that most sites on the outer (010) surfaces of MFI have similar acid strength to those at internal or bulk positions. Ensemble average DPE values on external surface sites (1486−1543 kJ mol^{-1}) are mostly similar to those at internal sites (1477−1506 kJ mol^{-1}) on the MFI surface model, and ensemble averaged DHE values (457−483 kJ mol^{-1}) are also similar to their bulk counterparts (457−476 kJ mol^{-1}). Al substitution at terminal silanol groups (SiOH) on the outer zeolite surface yields Lewis acidic Al, resulting in different acid strengths at those sites, but such sites represent a minority of surface T-sites. Unlike DPE and DHE, ΔE_{NH_3} probes a combination of acid strength and confinement because a gas-phase species enters the zeolite pores. Ensemble average ΔE_{NH_3} values indicate that most sites bind NH_3 as strongly on the surface (−160 to −113 kJ mol^{-1}) as bulk sites (−160 to −133 kJ mol^{-1}), despite the reduced confinement on surface sites. These ΔE_{NH_3} change very little on the MFI surface because most surface sites are within pockets that retain enough of the zeolite pore to solvate the NH_4^+ cations that form when NH_3 binds. Some sites, however, bind NH_3 more weakly if the solvating pore is absent or if NH_3 binds and deprotonates the H_2O on a Lewis acidic Al. Together, these data suggest that fully coordinated Brønsted acidic Al sites on the outside of zeolite crystals possess similar acid strength to those within the crystal and that many surface sites effectively confine an NH_4^+ cation. Such partial confinement on external sites indicates that NH_3 adsorption experiments are ineffective for broadly distinguishing between internal and external sites in MFI materials.

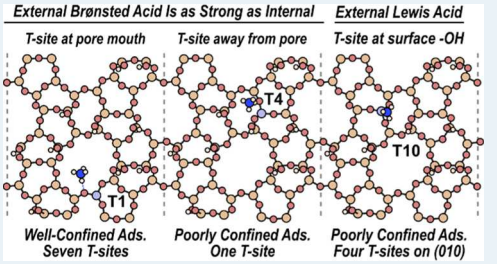

KEYWORDS: *zeolites, silanol groups, Brønsted acid strength, Lewis acid strength, adsorption, Thiele modulus*

1. INTRODUCTION

Zeolites are microporous crystalline materials primarily composed of tetrahedral sites (T-sites), where Al^{3+} substitution for Si^{4+} produces an anion that can be balanced by a proton (H^+) to form a Brønsted acid site. Because their small voids are of a similar size to molecules, zeolites are often used as shape-selective catalysts in the petrochemical industry—most notably in fluid catalytic cracking processes.[1−3] These voids can exclude molecules that are too large to diffuse through them, yielding high selectivity to desired products;[4,5] for example, in the production of *para*-xylene in MFI.[6−8] Similarly, reactions can be sterically limited by zeolite pores, constraining transition states to produce specific products in alkane cracking and dehydrogenation reactions,[9,10] methanol-to-hydrocarbon (MTH) processes,[11−16] alkene oligomerization,[17] or biomass upgrading.[18−20] Finally, zeolite pores stabilize reactive intermediates through non-covalent interactions—a combination of dispersive and van der Waals forces—that increase reaction rates as pore sizes approach the size of the relevant transition state.[21−23] Brønsted acid sites can be present both within zeolite pores, where these confinement effects dominate reactivity, and at the external surface of zeolite crystals whose surface area to volume ratios depend on the crystal size, morphology, and the presence of features such as mesopores,[24,25] pillars,[26−28] or fins.[29,30]

The strength of the Brønsted acid sites in zeolites partly dictates the reactivity of zeolite catalysts. Brønsted acid

Received: January 5, 2023
Revised: February 27, 2023
Published: March 20, 2023

strength can be calculated using deprotonation energy (DPE), which is the energy to remove a proton to a non-interacting distance by heterolytically cleaving its bond to the zeolite

$$HZ \rightarrow H^+ + Z^- \quad (1)$$

where higher DPE values indicate weaker acid sites. DPE depends on the trivalent heteroatom that substitutes Si^{4+} to form the Brønsted acid site, with DPE increasing (and acid strength decreasing) in the order $Al^{3+} < Fe^{3+} \approx Ga^{3+} < B^{3+}$.[31−33] First-order rate constants for methanol dehydration to dimethyl ether (DME) increase exponentially as DPE decreases with these different heteroatom substitutes in MFI[31] and with different heteroatoms in polyoxometalates (POMs) with a Keggin structure[22] (433 K, 0.2−20 kPa CH_3OH). Therefore, DPE is an important metric for predicting turnover rates and assessing the reactivity of heterogeneous Brønsted acid catalysts.

Periodic density functional theory (DFT) calculations on a suite of zeolites indicated that their DPE values remain nearly constant (generally varying by <25 kJ mol^{-1}) across all topologies (CHA, MFI, BEA, FER, MOR, and FAU) and within distinct T-sites in each topology.[34] Importantly, DPE estimates from periodic DFT calculations depend on the framework density, which alters the dielectric constant and, therefore, the predicted stability of the anionic conjugate base.[34,35] Additionally, spurious charge−charge interactions across the unit cell boundaries in periodic calculations can change DPE without changing the framework density.[36]

Similarly, dehydrogenation energy (DHE) is also a metric of acid strength, albeit indirectly, that captures the energy associated with homolytically cleaving the bond between the surface proton and the zeolite framework

$$HZ \rightarrow H^\bullet + Z^\bullet \quad (2)$$

Critically, DHE does not suffer from the periodic charge−charge interaction effects of DPE[36] and thus can be calculated without artifacts in periodic DFT methods and across zeolites with different framework densities and dielectric constants.

The binding energy of NH_3 (and other bases) is another common metric of acid strength and, unlike DPE and DHE, can be measured experimentally. This method measures the energy to adsorb NH_3 to a Brønsted acid site and form NH_4^+ near the anionic conjugate base

$$NH_{3(g)} + HZ \rightarrow NH_4^+\text{-}Z^- \quad (3)$$

Like DPE, NH_3 binding energy (NH_3 BE) measures the energy to heterolytically cleave the H−Z bond, and like DHE, it also avoids calculations with a net charge. However, NH_3 adsorption energies also reflect differences in confinement effects (i.e., van der Waals interactions and H-bonding to the zeolite framework) that lead to differences in NH_3 BEs with the environment surrounding the Al conjugate base, whereas DPE and DHE strictly measure the strength of the H−Z bond. Previous studies using temperature-programmed desorption and DFT have shown that base binding energies depend on the topology of the zeolite and the type of the base used,[37−40] despite similarities in their DPE values.[34] Generally, NH_3 binds more strongly in zeolites with smaller pores (e.g., FER) than those with larger voids (e.g., FAU), with particularly strong binding in the 8-membered ring (8-MR) of MOR.[37,41,42] Therefore, NH_3 BEs measure a combination of confinement and acid strength, although NH_3 is a relatively small probe that discriminates between different confining voids less than larger bases like pyridine. The use of base adsorption to measure the acidity of homogeneous Brønsted acids is common, where the solvent is identical across different acid molecules, acids are free to diffuse throughout the solution, and the concentration of hydronium ions (H_3O^+) depends on the concentration of acid molecules and the strength of the proton's bond to its conjugate base. In contrast, zeolites solvate base molecules differently depending on their pore shapes and sizes, producing different turnover rates despite similar H−Z bond strengths.[21,34] While the strength of base adsorption may correlate more closely with turnover rates for some reactions in zeolites than DPE or DHE, that correlation occurs because DPE and DHE vary little across different zeolite frameworks and because base adsorption also captures the solvating effects of the surrounding framework. Base adsorption can also be appealing because computed values can be compared to experimental observations; however, the same catalyst can yield different desorption behavior depending on the apparatus design, yielding inconsistencies across different experiments.[43−46] As such, computational studies of Brønsted acid strength in zeolites should combine each of these metrics (DPE, DHE, and NH_3 BE) to counter their respective weaknesses.[36,47]

Recent developments in zeolite synthesis can selectively produce pillared,[28,48−50] finned,[29] and other mesoporous or 2D zeolites[26,27,51−53] with larger external surface area to volume ratios and shorter diffusion lengths for reactants. These structural changes permit faster diffusion of bulky aromatics during the MTH process,[29,51,54] leading to slower deactivation and reduced propagation of the aromatics cycle. Additionally, recent strategies to specifically insert framework Al near the edges of zeolite crystals with an egg-shell design also increase catalyst lifetime during the MTH process and may lead to higher fractions of surface Brønsted acid sites.[55,56] The differences in deactivation rates for zeolites with shorter diffusion lengths to acid sites, however, raise questions about the differences in reactivity between sites within and near the surfaces of zeolite crystals. Experimental studies examining the differences between internal and external sites have indicated that external acid sites have slightly higher rates than internal sites for reactions involving bulky intermediates such as diphenylmethane formation[57] and Friedel−Crafts alkylation of benzene[58,59] and 1,3,5-trimethyl benzene.[60−63] For reactions forming smaller species like ethanol dehydration and propane cracking, self-pillared MWW and MFI zeolites with higher fractions of external sites have similar turnover rates to traditional zeolite samples.[64] These studies do not deconvolute the effects of acid strength, confinement, and Al position on internal and external sites, which can only be done rigorously using theoretical approaches. These differences in turnover rates for reactions with bulky intermediates result from differences in confinement and differences (if any) in Brønsted acid strength present at these external Brønsted acid sites. If acid strength does not change with Al nearer the surface of these zeolites, increasing surface area could provide a method to tune confinement within one zeolite framework independent of acid strength.

Prior studies have shown that the external surfaces of typical coffin-shaped MFI crystals terminate in silanol groups predominantly along their (010), (100), and (101) directions.[65−69] These silanol groups (SiOH) can form H-bonds to adsorbates and lead to distinct reactivity and adsorbate clustering within zeolite pores.[70,71] Additionally, SiOH groups

https://doi.org/10.1021/acscatal.3c00076
ACS Catal. 2023, 13, 4470−4487

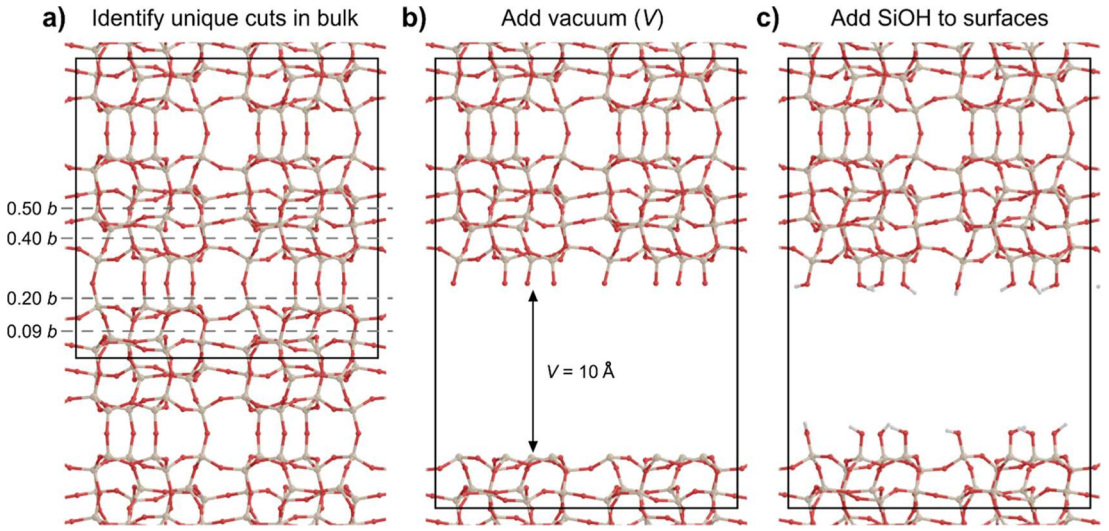

Figure 1. Illustration of the process of creating MFI surface models by (a) identifying the unique positions at which surfaces can terminate [shown here for the *b*-vector or (010) surfaces], (b) adding a vacuum layer (shown here with 10 Å), and (c) terminating the surface with silanol (SiOH) groups where appropriate.

could possess weak Brønsted acid character, although DPE values of these sites are up to 200 kJ mol^{-1} higher than on Brønsted acid sites arising from framework Al substitution, the latter of which are similar in strength to homogeneous superacids (e.g., HPF_6).[72] On zeolite surfaces, Al substitution at these sites can lead to 3-fold coordinated Lewis acid sites that bind H_2O.[65,66] Previous theoretical studies have found that external Lewis sites on BEA cannot stabilize carbocations upon isobutene adsorption as readily as Brønsted acid sites within the bulk of the zeolite.[66] In contrast, others have found that pyridine binding energies on external Brønsted acid sites of MFI are similar to or slightly weaker than (−215 to −167 kJ mol^{-1}) those on the T5 site in the bulk (−213 kJ mol^{-1}).[65] Similar calculations for the adsorption of H_2O, CH_3OH, DME, and pyridine as well as methanol dehydration to DME barriers on external sites in CHA indicated that bulk and external Brønsted acid sites differ little but that external Lewis acid sites bind basic molecules much more strongly than Brønsted acid sites.[73] However, no previous studies have examined the acid strength of these sites using a combination of DPE, DHE, and NH_3 BE, which may yield different insights from base adsorption calculations alone. Weaker base adsorption should occur on external sites because they are less confined than their bulk counterparts; however, only DPE and DHE calculations can determine if the strength of H−Z bonds of these external sites is different. Therefore, an assessment of the strength of these acid sites and a comparison between their strength and that of sites in the zeolite bulk are needed.

Here, we use a combination of DPE, DHE, and NH_3 BEs to compare all 12 bulk T-sites to all unique Al substitution locations on the most stable (010) surface of MFI. These calculations indicate that Brønsted acid sites that form at the surfaces of these zeolites do not differ significantly in DPE or DHE unless deprotonation occurs from H_2O bound to the otherwise trigonal planar Al. H_2O on these trigonal planar Lewis acidic Al sites has O−H bonds that are similar in strength to other Brønsted acidic O−H bonds based on DHE values, but their DPE values are much higher than those of other sites. This finding suggests that these sites do not stabilize anionic charge as well as other Brønsted acid sites if H_2O bound to a Lewis site is deprotonated. Together, these results show that most sites near the surface of the zeolite crystal have similar acid strength to those within the bulk unless Al substitution produces a Lewis acidic Al.

2. COMPUTATIONAL METHODS AND MODELS

All DFT calculations were performed using the Vienna ab initio simulation package (VASP)[74−77] implemented in the computational catalysis interface (CCI).[78] All calculations used the Perdew−Burke−Ernzerhof form of the generalized gradient approximation[79] with dispersive interactions modeled using the DFT-D3 method with Becke−Johnson damping (D3BJ).[80,81] While PBE-D3BJ does not predict barriers for the reaction in zeolites as accurately as CCSD(T) in cluster models,[82] this method does capture trends across and within materials relatively well.[83] While it is less accurate than more expensive methods like hybrid functionals, CCSD(T), and MP2, we believe that this functional adequately captures the trends within MFI and between the models we evaluate in this work. Planewaves were constructed using the projector-augmented wave (PAW) method with an energy cutoff of 400 eV.[84,85] The Brillouin zone was sampled only at the Γ-point. Optimization calculations used a multi-step process available in CCI. In the first step, wavefunctions were converged until they varied by $<10^{-4}$ eV, with forces calculated using a fast Fourier transform (FFT) grid 1.5× the plane wave cutoff. In the second step, wavefunctions were converged to $<10^{-6}$ eV with an FFT grid 2× the plane wave cutoff. Structural optimization continued until the forces on all atoms were <0.05 eV $Å^{-1}$. Gas-phase species were modeled in 18 × 18 × 18 $Å^3$ unit cells. The energy of a gas-phase proton was modeled with a partial electron (NELECT = 0.001 in the VASP INCAR) because otherwise such protons would not have any electron density for DFT to compute. Radical species (including the $H^•$ and $Z^•$) were calculated with spin polarization.

The MFI model used in this work was developed from the X-ray diffraction data of van Koningsveld et al., with the *Pnma* space group and unit cell parameters a = 20.078 Å, b = 19.894 Å, c = 13.372 Å, and $\alpha = \beta = \gamma = 90.0°$.[86] T-site numbering was

https://doi.org/10.1021/acscatal.3c00076
ACS Catal. 2023, 13, 4470−4487

adapted from the international zeolite association.[87,88] MFI has straight and sinusoidal 10-MR that intersect to form larger voids. Some MFI models are prone to restructuring during DFT calculations, introducing artifacts that alter predictions of barrier heights; however, this MFI model is sufficiently stable for studies of its catalytic properties.[89] We create MFI surface models by inserting vacuum regions (10 Å unless otherwise specified) in the [010] directions at unique cleavage locations within the unit cell (Figure 1a,b). After the vacuum is added, all dangling bonds are replaced with silanol groups (Figure 1c). The surface formed by cutting 20% along the *b*-vector (labeled 0.20 *b* in Figure 1a) produces the fewest dangling bonds upon cleavage, which we focus on in this work.

We study the Brønsted acid sites of the bulk MFI model shown in Figure 1a by substituting Al at all 12 unique T-sites. Protons and NH_4^+ cations were placed at each of the 4 O sites around each T-site. These cations were systematically reoriented around the T-site, as in previous studies,[8,36] which can significantly reduce the calculated energies. Protons and the O atoms to which they were attached were rotated around the axis produced by the adjacent Si and Al atoms in 30° increments. Similarly, NH_4^+ cations and the O atoms they deprotonated were rotated around the Si−Al axis in 30° increments. Additionally, the NH_4^+ cations were rotated around the axis formed by the H-bond between the framework O that was deprotonated and the nearest H atom of NH_4^+. Such systematic reorientations procedures rigorously probe the potential energy surface around each T-site and increase the likelihood of identifying configurations that are closer to the global minimum for a given state.

There are 24 unique T-site positions where we substitute Al on the cleaved surface model: 12 sites near the surface and 12 more at interior positions (these sets of 12 correspond to T1−T12 of the bulk). We denote the first set of sites as "external" T-sites and the latter as "internal" sites and contrast both with their "bulk" equivalents where no surface has been cleaved. We use three metrics to assess Brønsted acid strength in this work: DPE, DHE, and NH_3 BE (Scheme 1). We calculate DPE as

$$\mathrm{DPE} = E_{Z^-} + E_{H^+} - E_{HZ} \tag{4}$$

Scheme 1. Metrics for Assessing Brønsted Acid Strength

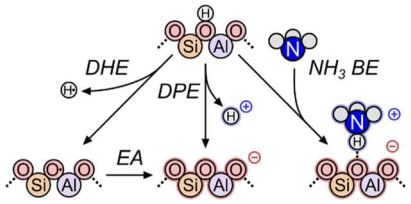

where E_{Z^-} is the energy of the deprotonated zeolite (the conjugate base), E_{H^+} is the energy of a gas-phase proton, and E_{HZ} is the energy of the protonated zeolite, matching the reaction shown in eq 1. Similarly, DHE values were calculated as

$$\mathrm{DHE} = E_{Z^\bullet} + E_{H^\bullet} - E_{HZ} \tag{5}$$

where $E_{Z^\bullet}$ is the energy of the dehydrogenated zeolite (the conjugate base) and $E_{H^\bullet}$ is the energy of a gas-phase hydrogen radical, matching the reaction in eq 2. Finally, NH_3 BE (ΔE_{NH_3}) is the difference between the NH_4-form zeolite and the gas-phase NH_3 and the proton-form zeolite

$$\Delta E_{NH_3} = E_{NH_4\text{-}Z} - E_{NH_3(g)} - E_{HZ} \tag{6}$$

where $E_{NH_4\text{-}Z}$ is the energy of the NH_4-form zeolite and $E_{NH_3(g)}$ is the energy of the gas-phase NH_3, matching the reaction in eq 3. We assume that protons and NH_4^+ cations rapidly exchange between the distinct O atoms associated with a given T-site and thus that these positions are equilibrated. For protons, this exchange is likely adsorbate-facilitated.[90−92] We calculate Boltzmann or ensemble average energies for these equilibrated proton or NH_4^+ positions

$$\langle E \rangle = \frac{\sum_{i=1}^{4} E_i e^{-E_i/k_B T}}{\sum_{i=1}^{4} e^{-E_i/k_B T}} \tag{7}$$

where E_i is the energy of the configuration associated with the O atom *i*, k_B is Boltzmann's constant, and *T* is the temperature. We use 415 K for these ensemble average calculations, which matches our previous studies in zeolites,[36,93−95] but our conclusions are not very sensitive to this temperature choice. The ensemble average DPE, DHE, or NH_3 BE values are calculated by taking the difference between the ensemble for equilibrated states and the absolute energies of other states. For example, ensemble average DPE is

$$\langle \mathrm{DPE} \rangle = E_{Z^-} + E_{H^+} - \langle E_{HZ} \rangle \tag{8}$$

while ensemble average NH_3 BE is

$$\langle \Delta E_{NH_3} \rangle = \langle E_{NH_4\text{-}Z} \rangle - E_{NH_3(g)} - \langle E_{HZ} \rangle \tag{9}$$

because the bound NH_4^+ and proton positions are both equilibrated.

When Al is substituted at hydroxylated positions at the zeolite's external surface, it can produce Lewis acidic, trigonal planar Al species that bind H_2O.[65,68,73,96] Specifically, these Lewis acidic sites can form at T7, T9, T10, and T12 positions on the surface model that we study in this work (Figure 1). H_2O bound to these sites can also act as a Brønsted acid (whose acid strength we calculate in this work), or H_2O can desorb and Al can behave as a Lewis acid. We analyze these sites using metrics already discussed (DPE, DHE, and NH_3 BE) when H_2O is bound and also assess H_2O binding energies (H_2O BEs), electron affinities (EAs), and NH_3 BE to the Lewis acidic Al (Scheme 2) as metrics of Lewis acid strength.

3. RESULTS AND DISCUSSION

3.1. DPE, DHE, and NH_3 BE at Bulk MFI Sites. We begin by discussing the relative stability of a proton at all O atom locations for all 12 T-sites in the MFI bulk model (Figure 2).

Scheme 2. Metrics for Assessing Lewis and Brønsted Acid Strengths on External Sites That Can Form H_2O

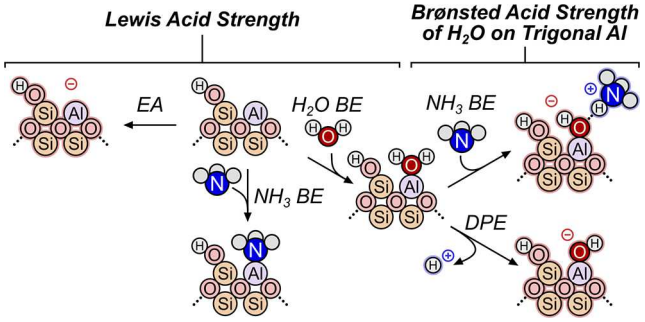

https://doi.org/10.1021/acscatal.3c00076
ACS Catal. 2023, 13, 4470−4487

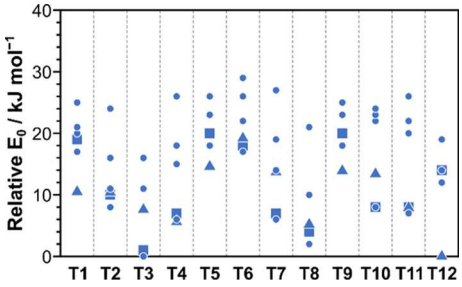

Figure 2. Relative E_0 for the protons on all four O atoms for each of the 12 T-Sites in the bulk MFI model (blue ●), the ensemble average relative E_0 for all protons on each T-site (blue ■; eq 7), and the relative energy of the deprotonated T-site (blue ▲), all in kJ mol^{-1}.

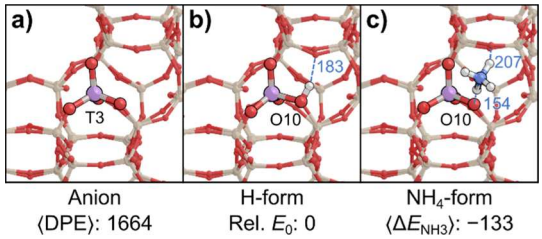

Figure 3. (a) Deprotonated anion form, (b) most stable H-form, and (c) most stable NH_4-form on T3 of the bulk MFI model. H-bonds in (b,c) are shown with blue dashed lines, and their lengths are denoted in pm.

These H-form stabilities are part of all the acid strength metrics used in this work—they are the reactant states in DPE, DHE, and NH_3 BE calculations—and, therefore, contribute to the differences in observed acid strength of T-sites in MFI. The most stable proton location across all 26 T-O site ensembles is on O10 with Al substituted in the T3 position, from which the relative stabilities of all other configurations are calculated (Figure 2). The relative stabilities of protons on different O atoms range up to 29 kJ mol^{-1} across all T-sites in MFI, and relative energies of protons at distinct O within a given T-site can vary by up to 20 kJ mol^{-1} with the largest ranges at T4, T7, and T8 and the narrowest ranges at T1, T9, and T12. Ensemble average stabilities (eq 7) tend to be close to the most stable position for each T-site because proton positions >5 kJ mol^{-1} less stable than the best at a given T-site contribute negligibly to the ensemble average at 415 K. This finding is consistent with previous DFT calculations on MFI and other zeolites showing that ensemble average stabilities are extremely close to the stability of the best proton location.[34,36]

The stability of protons in these different locations is determined both by the local environment of the proton and by the energy to substitute Al into the associated T-site location. The relative energies of the anionic MFI framework with Al substituted at all 12 T-sites are shown in Table 1 and Figure 2. While T12 is the most thermodynamically favorable location for Al substitution absent a cation,[97] an Al at T3 is within 10 kJ mol^{-1} and forms the most stable H-form structure (Figure 3b). This discrepancy between proton-form and conjugate base stabilities indicates that proton-form stabilities reflect the ability of a H to favorably interact with the surrounding framework and do not accurately reflect the thermodynamic preference to site Al in a particular position. In other words, even a cation as small as a proton is sensitive to the local framework topology because each T-site solvates protons differently depending on where those protons can be positioned. While the surrounding void environments affect the dispersive stability provided for larger adsorbates and cations, protons can sense the surrounding framework primarily through H-bonding interactions with bridging O at nearby locations.[36] These H-bonds are sometimes overlooked in DFT studies that do not consider a wide range of OH bond angles in their assessment of protonated T-sites in zeolites but are observed in our work because of the systematic reorientations we perform (Section 2).[8,36] Protons oriented within small 5- and 6-MR where such H-bonds are favorable were the most stable for all T-sites except T5 and T12 (Figures S1−S3, Supporting Information). Reorienting the protons on each O atom of T5 and T12 into a small ring incurs an energy cost. As a result, these T-sites prefer protons that are not in small rings despite the presence of such rings. Despite these costs, the most stable positions are only 5 and 2 kJ mol^{-1} more stable than the next most stable positions where the proton is in a small ring on T5 and T12, respectively. Previous studies have also found that the stabilities of Al arrangements in zeolites with their organic and inorganic structure-directing agents still present in the pores differ in stability from the proton forms.[97−101] These findings further indicate that proton-form stabilities cannot be used to infer Al positions in synthesized zeolites (in addition to the kinetic factors that could influence Al siting during zeolite crystallization). We calculate DPE and DHE at all T-sites and O atoms in MFI to capture how these proton solvation effects alter acid strength irrespective of the relative stability of the location for Al substitution.

DPE values range from 1638 to 1664 kJ mol^{-1} across all O-atoms for all 12 T-sites within the MFI bulk (Figure 4). These values are similar to those calculated for MFI sites in previous work using periodic DFT (1621−1668 kJ mol^{-1}; RPBE, PAW)[34] but higher than those from cluster models using DFT (1226 kJ mol^{-1} at T12; ωB97X-D, double-ζ 6-31G(d,p) basis set).[31] The higher DPE values from these calculations on periodic MFI occur because of spurious interactions across boundary conditions between anions in charged periodic calculations,[36] which are absent from cluster calculations, and because the densities of zeolite frameworks differ, which alters their dielectric constants.[35] Together, these differences mean that DPEs in different frameworks and across different

Table 1. Accessible Void Environments in MFI at Each T-Site[a]

	nearby void environment(s)			
T-site	int.	str.	sin.	ΔE_{Al^-} kJ mol^{-1}
T1	X	X	X	12
T2	X	X	X	5
T3	X	X	X	7
T4			X	5
T5	X	X		15
T6	X	X	X	22
T7	X	X		13
T8	X	X		4
T9	X	X	X	14
T10	X		X	15
T11	X	X		6
T12	X	X	X	0

[a]Adapted from Nimlos et al.[97]

https://doi.org/10.1021/acscatal.3c00076
ACS Catal. 2023, 13, 4470−4487

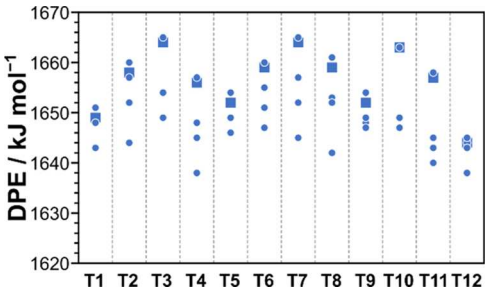

Figure 4. DPE (kJ mol^{-1}, eq 4) for each individual O atom (blue ●) and the ensemble averaged value (blue ■; eq 8) for all 12 T-Sites in bulk MFI.

methods (periodic vs cluster or embedded cluster) cannot be directly compared without corrections; however, comparisons between acid sites within a single framework are reasonable because the size of the unit cell is invariant in such analyses.

The ensemble average DPE value is closest to the highest DPE for each T-site because the highest DPE corresponds to the most stable proton position, which is also the most occupied state. Critically, the ensemble average DPE value most closely reflects the acid strength of each T-site as protons are expected to be able to rapidly exchange between O atoms in the presence of proton-shuttling adsorbates. T12 has the lowest ensemble average DPE (1644 kJ mol^{-1})—and therefore is the strongest acid site in MFI—because it has the most stable anion form and relatively unstable protons. In contrast, the ensemble average DPE values for T3 (1664 kJ mol^{-1}), T7 (1664 kJ mol^{-1}), and T10 (1663 kJ mol^{-1}) are the highest, indicating that these are the weakest acid sites. These sites either have very stable protons (T3; Figure 3a,b) or form relatively unstable anions (T7 and T10). This reflects the importance of the stabilities of both the proton (and any intrazeolite H-bonds it can form) and anion in determining DPE. Neither the proton stability nor the anion stability is the dominant factor governing DPE values in zeolite frameworks.

Importantly, prior studies have shown that increases in DPE do not produce equal increases in DFT-computed barriers to form cationic methanol dehydration transition states relative to the bare proton site on POMs ($H_{8-n}X^{n+}W_{12}O_{40}$, X = S, P, Si, Al, and Co).[22] For example, an increase in DPE by 1 kJ mol^{-1} leads to an increase in the methanol dehydration barrier of ~0.4 kJ mol^{-1}. These findings matched kinetic studies of turnover rates per H^+ on these POMs for methanol dehydration (0.2−20 kPa CH_3OH, 433 K). Similar findings hold based on experimentally measured turnover rates (per H^+) of methanol dehydration with different heteroatoms in MFI zeolites,[31] methylcyclohexane ring contraction and alkene isomerization on POMs and zeolites within bifunctional catalysts,[102−104] and formaldehyde and alkenes in H-SSZ-13 and H-SAPO-34.[105] Subsequent studies have indicated that this is because transition state formation on Brønsted acids also includes protonation of an adsorbate, ion−pair interactions between the transition state and conjugate base, and charge rearrangement that alters other covalent bonds in the transition state and catalyst.[106−108] As such, while ensemble average DPE values differ by 20 kJ mol^{-1} among T-sites within the bulk of MFI, such shifts in DPE would only lead to barrier height differences of 4−8 kJ mol^{-1}. Despite these modest changes, some reactions have shown significant Al site preference. For example, DME carbonylation occurs specifically at T3 in MOR;[109−111] however, this site specificity is caused by the local environment around each site (i.e., 12-MR regions vs 8-MR side pockets). Indeed, we concur with prior studies of DPE across many zeolite frameworks[34] and subsequent kinetic studies[21] that identified confinement as the key factor that determines turnover rates for aluminosilicate zeolites. The results of these studies indicated that acid strength can be considered constant across zeolite frameworks despite slight differences in DPE between different Al locations. As such, the 20 kJ mol^{-1} difference reported here between ensemble average DPE values for Al at different T-sites alone is unlikely to substantially alter reactivities of Al present at those distinct T-sites.

Another metric for acid strength is DHE, which measures the energy to homolytically cleave the O−H bond of the H-form zeolite and thus avoids charged calculations that cause issues in periodic DFT software. The ensemble averages of DPE and DHE linearly correlate in the MFI bulk (Figure 5).

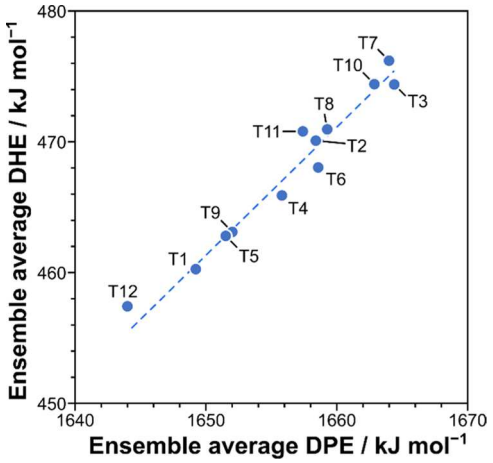

Figure 5. Ensemble averaged DHE shown as a function of ensemble averaged DPE, both in kJ mol^{-1}, for all 12 T-sites in bulk MFI.

These DPE and DHE values are related by the EAs of the zeolite conjugate base (EA_Z) and the gas-phase proton (EA_H)

$$DPE = DHE + EA_z - EA_H \quad (10)$$

Of these EAs, only EA_Z is a property of the zeolite and thus the Al atom location, while EA_H is a property of H radicals and protons in vacuum and is constant. Therefore, the slight scatter and excellent correlation in the trend between DPE and DHE arise because the EA_Z values are nearly constant across the 12 T-sites in MFI (−120 to −123 kJ mol^{-1}, Table S1, Supporting Information). This result indicates that DHE is an excellent alternative acid strength metric to DPE calculations—which are complicated by charge artifacts in periodic DFT codes—when EAs of the conjugate bases are expected to be nearly invariant.

NH_3 BE (ΔE_{NH_3}, eq 6) is another metric for acid strength, but one which convolutes both acid strength and confinement effects. ΔE_{NH_3} values are negative for most O atoms in the MFI bulk, reflecting the enthalpic benefit of NH_3 adsorption (Figure 6). NH_3 binds most strongly to O23 on T10, with a binding energy of −167 kJ mol^{-1}. The NH_4^+ cation in this structure is positioned within the sinusoidal channel and forms two H-bonds to other nearby framework O atoms (Figure S6, Supporting Information). T4 has the lowest ensemble average NH_3 BE. T4 is the only T-site that is not accessible from the

https://doi.org/10.1021/acscatal.3c00076
ACS Catal. 2023, 13, 4470−4487

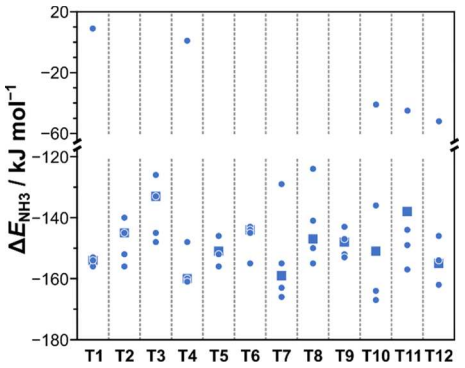

Figure 6. Individual O site (blue ●) and ensemble averaged (blue ■) NH_3 BE in kJ mol^{-1} for all 12 T-sites in the bulk MFI model.

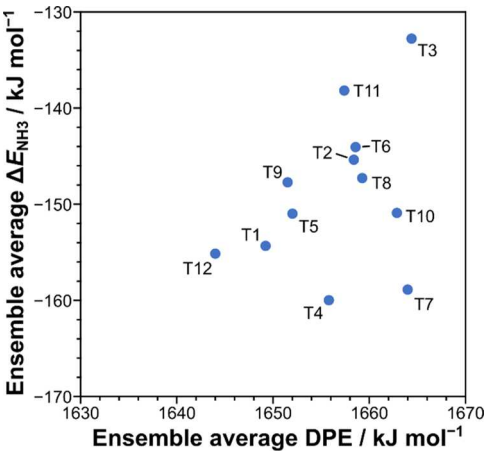

Figure 7. Ensemble average NH_3 BEs (ΔE_{NH_3}) as a function of the ensemble average DPE, both in kJ mol^{-1}, in bulk MFI.

intersection (Table 1), so its local environment is overall the best at stabilizing the cationic NH_4^+ via dispersive interactions. NH_3 binds most strongly to O12 on T4, where it also forms H-bonds to two other framework O atoms like the most stable NH_4^+ on O23 of T10. In contrast, the O4 positions around T1 and T4 have positive ΔE_{NH_3} values (+9 and +1 kJ mol^{-1}, respectively), while others have negative but much weaker binding energies (O20 on T8 and T12 and O24 on T10 and T11). These structures involve NH_4^+ cations in subunits of MFI for each of these O atoms (all NH_4-form structures in the bulk MFI model are shown in Figures S4−S6 of the Supporting Information). These O sites are essentially unoccupied by NH_4^+ cations and thus do not significantly influence ensemble average ΔE_{NH_3} values. The ranges of proton and NH_4^+ cation stabilities at different O atoms within the same T-site suggest that theoretical studies must examine all O atoms for a given T-site to reach accurate conclusions. Additionally, these large energy ranges for NH_4^+ interacting with different O atoms indicate the diversity of environments that are available at different O sites around each T-site.

Ensemble average ΔE_{NH_3} values vary from −160 to −132 kJ mol^{-1} across the 12 T-sites in MFI. This range of 28 kJ mol^{-1} is significantly larger than that observed for DPE (20 kJ mol^{-1}) or DHE (19 kJ mol^{-1}) and shows that the diversity of confinement among different Al locations is greater than the changes in acid strength. These NH_3 BEs do not correlate strongly with DPE or DHE because ammonia adsorption convolutes acid strength and confinement effects (Figures 7 and S7, Supporting Information). The effect of confining gas-phase NH_3 within the zeolite pore causes significant deviations from the expected correlation at T4, T7, and T10 (Figure 7). Notably, ΔE_{NH_3} is stronger for these sites than those with similar DPE values because when NH_3 adsorbs to these sites, it is better solvated than on others. T4, for example, is only accessible from the sinusoidal channel (Table 1). While it has a higher ensemble average DPE (1656 kJ mol^{-1})—and therefore forms a weaker acid site—than T5 or T9 (both 1652 kJ mol^{-1}), its ensemble average ΔE_{NH_3} is >8 kJ mol^{-1} stronger on T4 (−160 kJ mol^{-1}) than on T5 or T9 (−151 and −148 kJ mol^{-1}, respectively). Among the remaining sites, ΔE_{NH_3} does still partly correlate with DPE, indicating that proton stability does still affect ΔE_{NH_3}. For example, T3 has both the highest DPE (1664 kJ mol^{-1}) and the weakest ensemble average ΔE_{NH_3} (−133 kJ mol^{-1}). The relative energy of the most stable NH_4-form on T3 (20 kJ mol^{-1}), which binds to O10 like the most stable proton (Figure 3c), is near the average among all T-sites (16 kJ mol^{-1}). This provides further evidence that the stabilities of both the H-form and NH_4-form govern these binding energies, much like the H-form and conjugate base affect DPE values. However, the confinement effects that affect NH_3 adsorption make such measurements unreliable for quantifying acid strength despite some cases of agreement between DPE and ΔE_{NH_3}.

Together, these data suggest that acid strength depends weakly on the Al position within MFI. Ensemble average DPE and DHE—which most closely reflect the observable acid strength of sites from Al at specific T-site locations—vary by 20 and 19 kJ mol^{-1}, respectively, consistent with prior studies of DPE in MFI.[34] DPE and DHE values correlate strongly, indicating that the EA remains similar across Al locations within the zeolite. While the NH_3 BE is the only metric we use here that can be measured experimentally, it does not reliably indicate the energy to heterolytically cleave the O−H bond of the Brønsted acid site. Instead, it simultaneously includes bond cleavage and confinement effects upon NH_3 adsorption, which convolutes the estimates of Brønsted acid strength. This difference is most obvious for T-sites whose ensemble average DPE and ΔE_{NH_3} values do not match the linear trend of other sites (T4, T7, and T10). On these sites, NH_4^+ cations are solvated better than other sites and their ΔE_{NH_3} are lower than that of others with similar DPE values.

3.2. Deprotonation, Dehydrogenation, and NH_3 Binding on Surface Acid Sites. Next, we calculate the energies of protons at all possible unique locations on the most stable termination of the MFI structure in the [010] direction and compare them. The terminated MFI model contains two types of each T-site: internal and external. An external site is one that is on the surface of the cut, while an internal site is completely inside of the zeolite (Figure 8). In Section 2, we describe the formation of this surface model in more detail and that the chosen termination places Si−OH groups at T7, T9, T10, and T12. Substituting an Al at one of these external Si−OH positions results in an anionic Al−OH site, whose charge can be compensated by a proton. If the proton prefers to bind to the existing OH, then an Al−H_2O site forms, which can desorb H_2O to produce a trigonal planar, Lewis acidic AlO_3. At the other surface and all internal sites, Al remains tetrahedrally

https://doi.org/10.1021/acscatal.3c00076
ACS Catal. 2023, 13, 4470−4487

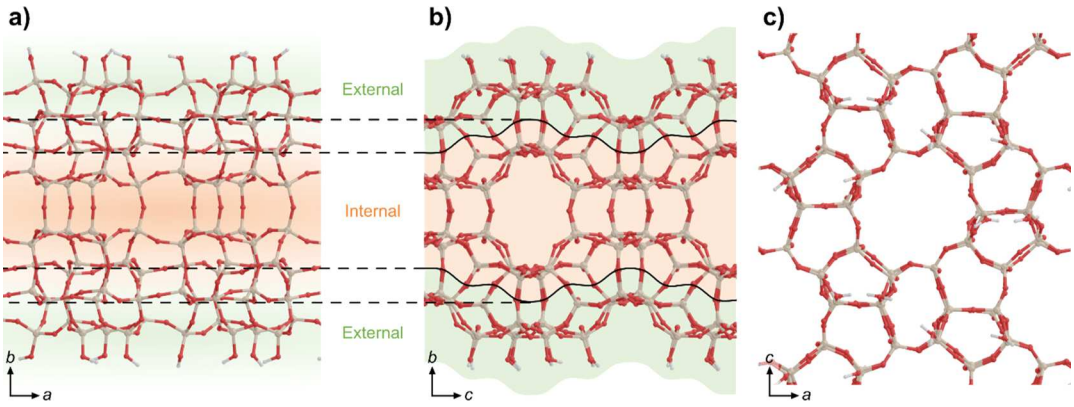

Figure 8. Locations of internal (orange) and external (green) T-sites on the (010) surface MFI model, shown (a) along the *c*-vector and (b) along the *a*-vector. (c) The same surface model shown along the *b*-vector.

coordinated and protons at such sites behave exclusively as Brønsted acids.

The bulk sites have a smaller range of relative energies than the sites on the surface model (Figure 9). Among sites on the surface model, the external sites have a larger range than the internal sites: both the most and least stable H-forms occur on external sites. The most stable proton position on the surface model overall forms on O23 of an external T10 site. When a proton is on this O, it forms H_2O bound to a Lewis acidic AlO_3 (Figure 10c). Three other T-sites are also capable of forming these H_2O-bound structures: T7, T9, and T12 (Figures S14 and S15, Supporting Information). In each case, the H_2O-bound structure is the most stable configuration for a proton around these external T-sites. The least stable site on the surface model is formed with a proton on O17 of T7, with a relative E_0 of 57 kJ mol^{-1}, which forms an Al site with two nearby OH groups—one pendant and one bridging two T-sites. Such configurations are generally much less stable on these T-sites, as indicated by the relative proton forms for external T7, T9, T10, and T12 sites in Figure 9. These data indicate that Al is the most stable when it forms trigonal planar Lewis acid sites bound to H_2O on the external surfaces of MFI.

Meanwhile, the internal sites have relative energies of 17−51 kJ mol^{-1}, which is a similar range (34 kJ mol^{-1}) to those of the bulk sites (29 kJ mol^{-1}). Their stabilities follow similar trends because the internal sites have a similar local structure to bulk sites but differ slightly because of the internal site proximity to the zeolite surface. In both cases, the most stable proton position is O10 on T3 and the least stable is O15 of T6. Such similarities in stability trends for internal and bulk sites indicate that their catalytic behaviors should be similar absent other

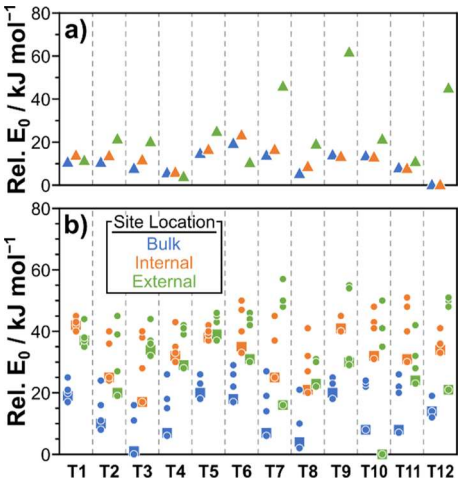

Figure 9. Relative E_0 in kJ mol^{-1} for (a) anions (▲) and (b) protons on all four individual O atoms (●), the ensemble averaged values (■) for each of the 12 T-sites in the bulk MFI (blue) and the 12 internal (orange) and 12 external (green) T-sites in the *y*-cut MFI model.

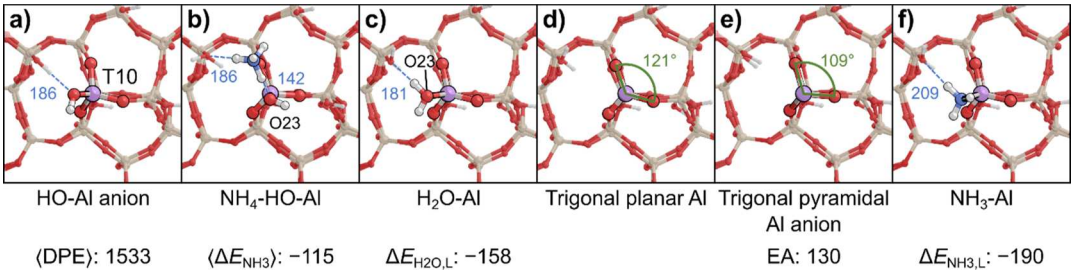

Figure 10. Structures for the external T10 site (a) after deprotonating the H_2O, (b) after adsorbing NH_3 to the H_2O−Al, (c) with H_2O bound to the Al, (d) after removing H_2O to form trigonal planar Al, (e) with an additional electron (which forms a trigonal pyramidal Al), and (f) with NH_3 bound directly to the Lewis acidic Al. Blue dashed lines show H-bonds in (a−c,f) with their distances labeled in pm. O−Al−O bond angles are shown in green for Lewis acidic Al in (d,e). Acid strength metrics are shown in kJ mol^{-1} below each relevant structure for the external T10 site—ensemble average DPE (⟨DPE⟩, see Figure 11), ensemble average NH_3 BE (⟨ΔE_{NH_3}⟩), Lewis acidic H_2O BE ($\Delta E_{H_2O,L}$), EA, and Lewis acidic NH_3 BE ($\Delta E_{NH_3,L}$).

https://doi.org/10.1021/acscatal.3c00076
ACS Catal. 2023, 13, 4470−4487

structural differences arising from the proximity to the zeolite surface.

DPE values on surface MFI models with 10 Å of vacuum space are 1477−1543 kJ mol^{-1} (Figure 11), which are 108−

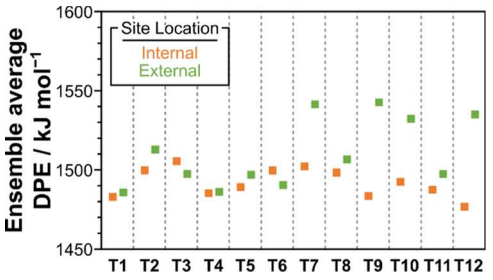

Figure 11. Ensemble average DPE values in kJ mol^{-1} for the internal T-sites (orange) and external T-sites (green) in the MFI surface model.

170 kJ mol^{-1} lower than those of equivalent sites of the bulk model. Theoretical studies of acid strength have indicated that DPE values can vary across zeolite frameworks according to their density (and therefore relative permittivity).[34,35] Our prior work also showed that the density of charge in periodic DFT calculations altered the calculated DPE values in CHA without significantly altering the dielectric constant of the underlying zeolite,[36] indicating that the distance between ionic centers in periodic DFT calculations can also alter DPE values. In other words, the size of the unit cell affects DPE values and adding 10 Å of vacuum space creates an artifact, preventing direct comparisons between our surface and bulk models. The similarity in structure and relative energy between the internal sites on the cleaved model and the bulk sites discussed earlier indicates that internal sites should have similar (if not identical) acid strength to bulk sites. The differences in the computed DPE values between internal sites on the cleaved model and bulk sites arises primarily because of differences in unit cell sizes and relative permittivity. As such, we compare the DPE values of internal and external sites to determine how Al proximity to the surface of the zeolite affects acid strength.

The four sites that form trigonal planar Lewis acidic Al with bound H_2O also have the highest ensemble average DPE values (1533−1543 kJ mol^{-1}). These DPE values are at least 19 kJ mol^{-1} higher than all external sites that do not form Lewis acids (1486−1513 kJ mol^{-1}) (Figure 12), a similar range to that of internal sites (1477−1506 kJ mol^{-1}). This similarity in DPE indicates that surface sites have similar Brønsted acid strength to internal sites unless they form a Lewis acid Al site with bound H_2O. Purely Brønsted acid sites that cannot form trigonal planar Al also tend to form much more stable anions than Al locations that form Lewis acid sites (Figure 9a). The three least stable anion positions are the external sites at T9 (62 kJ mol^{-1}), T7 (46 kJ mol^{-1}), and T12 (44 kJ mol^{-1}). While T10 also forms a Lewis acid, its anion is slightly more stable (21 kJ mol^{-1}; shown in Figure 10a) than the anions of external T4 and T2 and internal T6 (25, 21, and 23 kJ mol^{-1}, respectively). Notably, only these sites that form trigonal planar Al on the outer surface have DPE values that deviate by >15 kJ mol^{-1} in the surface model from their internal counterparts, with most differing by <10 kJ mol^{-1} (Figure 12).

Next, we assess DHE for sites on the surface model and compare them to the bulk model. DHE does not suffer from the same spurious charge−charge interactions in periodic

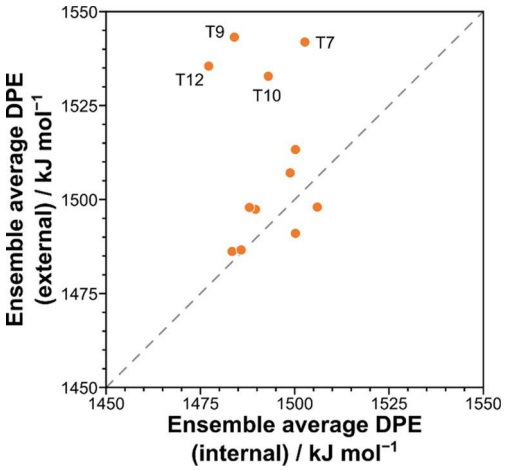

Figure 12. Ensemble average DPE for external sites as a function of their corresponding ensemble average DPE at the equivalent internal site in kJ mol^{-1}. The dashed gray line represents parity. T-sites that form trigonal planar Lewis acidic Al at the surface are individually labeled (T7, T9, T10, and T12).

calculations that DPE does.[36] Ensemble average DHE and DPE correlate linearly for bulk, external, and internal sites; however, the slope of the trendlines for the internal sites is 0.78, while that of the external sites is 0.33 (Figure 13). This

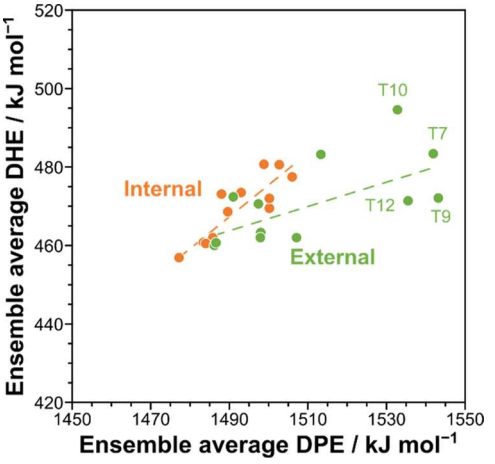

Figure 13. Ensemble average DHE as a function of ensemble average DPE (both in kJ mol^{-1}) of internal surface (orange) and external surface (green) T-sites. T-sites that form trigonal planar Lewis acidic Al at the surface are individually labeled (T7, T9, T10, and T12).

trend indicates that the DHE for bulk and internal sites behave similarly and that their acid strengths remain nearly identical. Meanwhile, the external Lewis sites have DHE values that are much closer (471−495 kJ mol^{-1}) to those of the bulk (457−476 kJ mol^{-1}), internal (457−481 kJ mol^{-1}), and other external (460−483 kJ mol^{-1}) sites. These data indicate that the strength of the O−H bonds of the H_2O bound to Lewis acidic Al sites is similar to those of other Brønsted acid sites but that the EA of these Lewis sites is much lower when there is a lingering OH group on the Al. This lower EA produces a much less stable conjugate base upon heterolytic cleavage of the O−H bonds than other Brønsted acid sites. As such, the ensemble average DPE values for these sites are much higher than those of all other sites.

https://doi.org/10.1021/acscatal.3c00076
ACS Catal. 2023, 13, 4470−4487

Together, these data suggest that DPE and DHE remain very similar regardless of Al proximity to the outer surfaces of the zeolite. One exception arises when Al is substituted into Si−OH groups at the edges of zeolite crystals, where it ultimately forms a trigonal planar Lewis acid site. As such, differences in reactivity between external and internal sites are likely caused by (1) diffusion constraints, (2) changes in confinement, or (3) the formation of Lewis acid sites. Next, we assess binding energies for NH_3 on these sites, which partly measures confinement at these different locations in addition to acid strength.

Ensemble average ΔE_{NH_3} values are similar for bulk and internal sites, remaining within 6 kJ mol^{-1} for all T-sites (Figures 14 and 15). These internal sites on the surface model retain similar local environments around each T-site to the bulk equivalent, and therefore, binding energies for NH_3 remain indistinguishable from those of the bulk model. On the other hand, NH_3 binding on equivalent external T-sites is much stronger than the bulk counterpart (T3), significantly weaker (T4, T7, T10, and T12), slightly weaker (T1, T2, T5, T9), or nearly identical (T6, T8, T11). No single factor disproportionately affects ΔE_{NH_3} and the expectation that all external sites would weakly bind NH_3 because of a relative lack of confinement is not supported by these data.

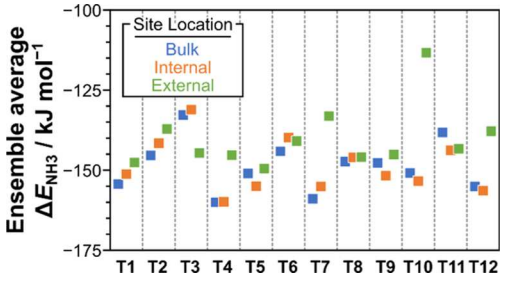

Figure 14. Ensemble average NH_3 BE (ΔE_{NH_3}) for all T-sites of the bulk model (blue) and the internal (orange) and external (green) T-sites of the (010) surface model in kJ mol^{-1}.

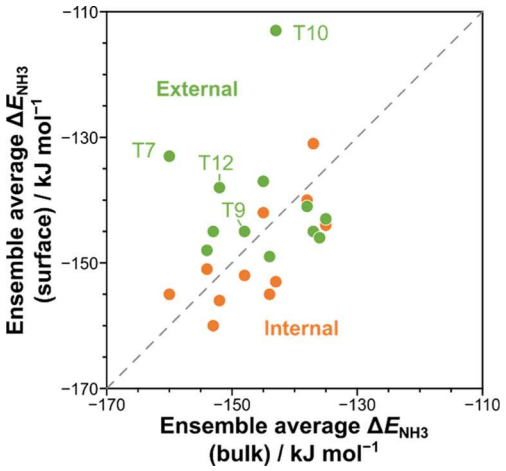

Figure 15. Ensemble average NH_3 BEs (ΔE_{NH_3}) in kJ mol^{-1} for the internal (orange) and external (green) T-sites as a function of the bulk ensemble average ΔE_{NH_3}. T-sites that form trigonal planar Lewis acidic Al at the surface are individually labeled (T7, T9, T10, and T12).

NH_3 binds weakly to H_2O−Al structures that form at external T-sites that can form Lewis acid sites (T7, T9, T10, and T12; an example structure for T10 is shown in Figure 10b), resulting in ΔE_{NH_3} values that are 7 to 40 kJ mol^{-1} weaker than their internal purely Brønsted acid counterparts. These shifts in ΔE_{NH_3} reflect a combination of weaker Brønsted acid strength and less confinement of the NH_4^+ cation. NH_3 also binds 15 kJ mol^{-1} more weakly to the external site than to the internal T4 site exclusively because the NH_4^+ is less confined on the external site. Thus, there is a significantly weaker binding of NH_3 when the T-site is placed at an external position than an internal position for less than half of these T-sites (5 of 12). These weaker binding energies are caused by less confined NH_4^+ cations and (for four T-sites) a weaker Brønsted acid.

The remaining seven external T-sites (T1, T2, T3, T5, T6, T8, and T11) are located at the pore mouths of the straight channels, and the bound NH_4^+ on these sites are solvated in the straight pore. As such, the solvation of these cations is similar to the solvation at corresponding internal sites. At external T1, T2, and T5 sites, the NH_4^+ cation is only slightly less confined than when bound to their internal analogues, resulting in weaker NH_3 adsorption by 4 to 6 kJ mol^{-1}. NH_3 adsorption energies for T6, T8, and T11 are nearly identical for the external and internal positions in the cleaved surface models (ΔE_{NH_3} vary by less than 2 kJ mol^{-1}). The remaining external site (T3) is the only site where NH_3 binds more strongly (by 17 kJ mol^{-1}) than its internal counterpart. NH_4^+ is the most stable on the same O10 atom as that on the bulk site, which can access the entrance to the straight pore of the zeolite (Figure S20, Supporting Information), similar to T6, T8, and T11 external sites. In contrast, the most stable proton position for the external T-site is on O9, where the proton resides in a 5-MR on the outer edge of the zeolite in a cup formed by the cleaved sinusoidal channel (Figure S12c, Supporting Information). This position is less stable than the preferential site for protons at internal or bulk T3 sites (O10), on which the proton is in a different 5-MR (Figure S1c, Supporting Information). This destabilizes the proton relative to the bound NH_4^+ cation, resulting in a more negative ΔE_{NH_3} value. Because these seven external T-sites (T1, T2, T3, T5, T6, T8, and T11) can still stabilize cations through Coulombic and H-bonding interactions, we cannot define external T-sites without nuance because the location of the Al may be a secondary factor to the location of the cations it stabilizes.

These DPE, DHE, and ΔE_{NH_3} metrics indicate that heterolytic O−H cleavage generally occurs much less favorably than homolytic cleavage on external sites when the cleaved bond is part of a H_2O−Al complex (T7, T9, T10, and T12 in this surface model). In other words, Al that can form a Lewis acidic site and bind H_2O can behave as a Brønsted acid with higher DPE and higher ΔE_{NH_3} values than other surface sites. Despite the higher energies for heterolytic O−H bond cleavage, H_2O on Lewis acidic Al has similar DHE values to other external sites. These Lewis acidic sites behave distinctly from Brønsted acid sites at the surface and must be evaluated using other metrics, which we address next. These data also indicate that other external sites (i.e., those that do not form at Si−OH species created by surface cleavage) have similar Brønsted acid strength to sites within the internal regions of surface or bulk MFI models. Furthermore, seven of these

https://doi.org/10.1021/acscatal.3c00076
ACS Catal. 2023, 13, 4470−4487

external sites (T1, T2, T3, T5, T6, T8, and T11) can stabilize cations by fully or nearly fully solvating them in adjacent pores. As such, these sites behave nearly identically to their internal counterparts by all metrics studied here.

3.3. Measuring Lewis Acid Strength with NH_3 Binding, H_2O Binding, and EA at Surface Sites. Like Brønsted acid strength, Lewis acid strength can be measured and quantified using binding energies of basic molecules (e.g., H_2O or NH_3). While generating the structures of Brønsted acid sites on the MFI surface model, we computed the energies of these Lewis acidic, trigonal planar Al species with a bound H_2O. One of the O−H bonds can be cleaved heterolytically or homolytically, or NH_3 can bind to this H_2O to form a NH_4^+−OH^- pair to measure Brønsted acid strength, as described in Section 3.2. Additionally, the H_2O can desorb or be replaced by NH_3 on the Al, both of which putatively measure the Lewis acid strength of the trigonal planar Al. While Brønsted or Lewis acid strength can be quantified using binding energies of bases, these binding energies also measure confinement, H-bonding, and other effects of the local environment. As such, binding energies alone do not purely measure acid strength like DPE, as we have shown in this work and our prior work.[36,47] A similar, adsorbate-free metric must also be used for the trigonal planar Lewis acid sites that we study in this work. Because Lewis acid sites accept electrons, EA should reflect the strength of these trigonal planar Al sites.

The EA of these Lewis acid sites can be measured by calculating the energy to add one electron to the site

$$\mathrm{EA} = E_{Z^-} - E_Z \quad (12)$$

where E_Z is the energy of the bare Lewis acid site and E_{Z^-} is the energy of the anionic site. These EA values are 128−146 kJ mol^{-1}, a similar range to that of the ensemble average DPE values of bulk MFI sites (1644−1664 kJ mol^{-1}). H_2O BEs to Lewis acidic Al ($\Delta E_{H_2O,L}$) and NH_3 BEs to Lewis sites ($\Delta E_{NH_3,L}$) can be compared to EA values like our comparisons of DPE and ΔE_{NH_3} in Sections 3.1 and 3.2. Such a comparison indicates that $\Delta E_{NH_3,L}$ and $\Delta E_{H_2O,L}$ do not correlate strongly with EA in this small data set (Figure 16), although $\Delta E_{NH_3,L}$ and $\Delta E_{H_2O,L}$ correlate with one another (Figure 17). $\Delta E_{H_2O,L}$ values are much weaker (−129 to −158 kJ mol^{-1}) than $\Delta E_{NH_3,L}$ (−171 to −190 kJ mol^{-1}) on these external sites. These stronger NH_3 BEs reflect the strength of NH_3 as a base relative to H_2O. The strong correlation between these binding energies indicates that these base molecules bind similarly in these environments and that either one could be appropriate for studying the Lewis acid strength of these external Al species. This strong agreement between the adsorption energies of probe molecules matches the behavior of dissociative adsorption energies in CHA with metals of different Lewis acid strength.[112] However, the absence of a strong correlation between binding energies and EA indicates that other adsorbate-free metrics that rigorously quantify Lewis acid strength may be necessary when studying these sites. Instead, these adsorption energies measure both the Lewis acid strength of the active site and the interaction of the adsorbate with the surrounding environment. Notably, when an electron is added or a base adsorbs to trigonal planar Al, it becomes trigonal pyramidal (Figure 10c−f). This geometric change indicates that each of these changes the hybridization of the Al similarly.

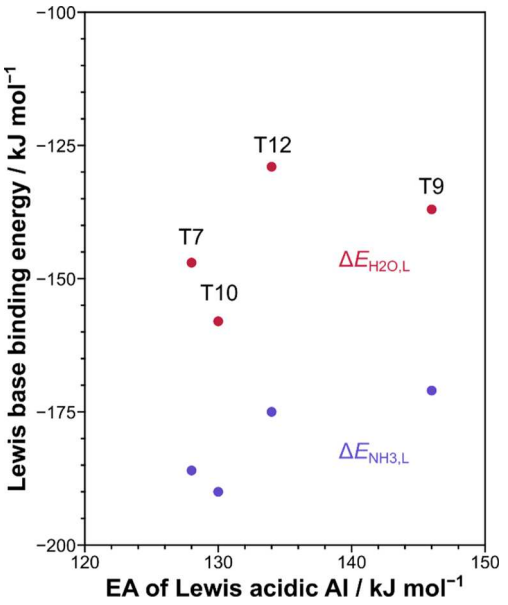

Figure 16. Binding energies for H_2O ($\Delta E_{H_2O,L}$, red) and NH_3 ($\Delta E_{NH_3,L}$, purple) as functions of the EA for each trigonal planar Lewis acidic Al position on the MFI surface model.

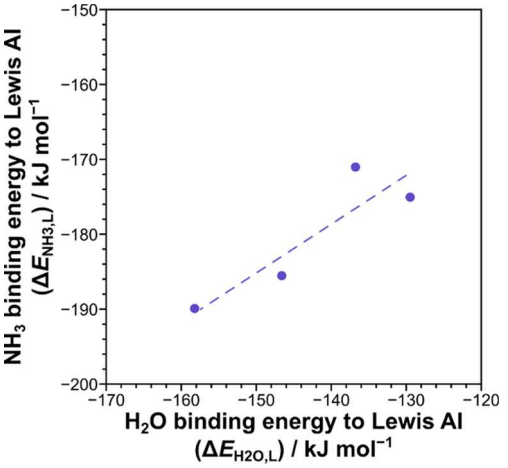

Figure 17. NH_3 BEs in kJ mol^{-1} to external Lewis acidic Al ($\Delta E_{NH_3,L}$) as a function of H_2O BEs to the same Lewis acidic Al (ΔE_{H_2O}). The dashed line represents a linear fit.

These H_2O and NH_3 BEs do not correlate strongly to DPE values calculated for Lewis acid Al with bound H_2O (Figure 18a). Instead, they correlate better with DHE and NH_3 BE where the NH_3 binds as a Brønsted base to the hydrated Lewis acid Al (Figure 18b,c). Ostensibly, these Lewis acid strength metrics should behave similarly for both DPE and ΔE_{NH_3}. Both DPE and NH_3 binding heterolytically cleave the O−H bond of the Lewis acid-bound H_2O and should correlate in the absence of strong confinement effects that strengthen NH_3 binding. However, among assessments of the Brønsted acid strength of the Lewis acid-bound H_2O, DHE appears to best predict the strength of Lewis base binding energies based on this limited data set. Notably, NH_3 binds much more strongly to Lewis acidic trigonal planar Al than it does to Brønsted acid sites within the bulk. NH_3 BEs to these Lewis sites are −190 to −171 kJ mol^{-1}, while no bulk Brønsted acid sites have ΔE_{NH_3}

https://doi.org/10.1021/acscatal.3c00076
ACS Catal. 2023, 13, 4470−4487

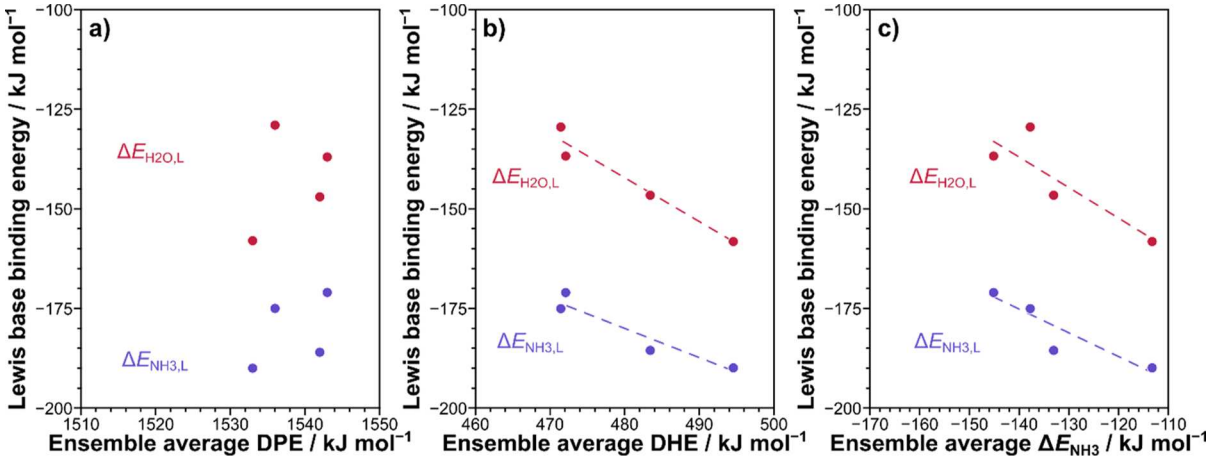

Figure 18. Binding energies of H_2O ($\Delta E_{H_2O,L}$) and NH_3 ($\Delta E_{NH_3,L}$) to external Lewis acidic Al sites on the MFI surface model as functions of (a) ensemble average DPE, (b) ensemble average DHE, and (c) ensemble average NH_3 BE (ΔE_{NH_3}) on the hydrated Lewis acid site. Dashed lines in (b,c) represent linear fits.

stronger than −160 kJ mol^{-1}. Finally, Lewis base binding energies negatively correlate with DHE and ΔE_{NH_3} (Figure 18b,c). Such a trend indicates that the more strongly bound H_2O has stronger O−H bonds. This contrasts with traditional bond order conservation models, which propose that stronger binding withdraws electrons from other bonds within an adsorbed molecule.

These data suggest that acid strength varies between external Lewis Al sites in similar magnitude to Brønsted acid strength between sites within the bulk of MFI, which should not produce substantial changes in turnover rates. Additionally, these external Lewis acid sites behave distinctly from other Al positions on the outer surfaces of MFI. This combination of EA—a possible adsorbate-free measurement of Lewis acid strength—with common adsorption metrics should fully characterize these external Lewis acidic Al sites. Such a combined approach that studies both the Brønsted acid strength of H_2O on Lewis acidic Al and the Lewis acid strength of the trigonal planar Al provides a comprehensive analysis of these unique external sites.

3.4. Contributions of External Sites to Observed Reaction Rates. Recent advances in zeolite synthesis have produced pillared,[28,48−50] finned,[29] and other mesoporous or 2D zeolites.[26,27,51−53] These materials have larger external surface area to volume ratios of the crystal (A_s/V) and, therefore, a higher fraction of external Brønsted acid sites. Here, we showed that these external sites have the same Brønsted acid strength as that of internal sites; however, such external sites confine surface intermediates and transition states less than internal sites and, therefore, tend to have higher reaction barriers and lower rate constants than internal sites. For example, the first-order rate constant for propene dimerization is ∼30× higher on TON than on a mesoporous aluminosilicate (SiAl) (10−400 kPa propene, 503 K), materials that our work shows should have similar Brønsted acid strengths.[23] This enhancement should approximately reflect the stability conferred by confinement and thus the ratio of k values on internal and external sites (k_{int}/k_{ext}) absent changes in Brønsted acid strength. Similar enhancements are observed when comparing acetone condensation on MCM-41 (a mesoporous SiAl material) and MFI ($k_{int}/k_{ext} \approx 85$; 473 K, 0.1−4 kPa acetone).[113] For methanol dehydration, rates between MFI and FAU have also been contrasted (one would expect FAU to offer minimal confinement), and the ratio of first-order rate constants is 8.5 (433 K, 0.1−20 kPa CH_3OH).[21] The relative ratios of these k values indicate a decrease in $\Delta G^{\ddagger}$ values of 8−18 kJ mol^{-1} from external to internal sites and suggest that confinement effects can influence rate constants, though up to a factor of 10^2, depending on the reaction of interest. Crucially, these measured effects of confinement (k-ratios) do not reflect changes in acid strength, as indicated by our DPE calculations in this work.

As the A_s/V and crystal habit change, the contribution of external and internal sites to the overall rate also changes. The ratio of rates on external to internal Brønsted sites (r_{ext}/r_{int}) is derived in Section S6 of the Supporting Information as

$$\frac{r_{ext}}{r_{int}} = \left(\frac{k_{ext}}{k_{int}}\right)\left(\frac{\rho_{T,ext}}{\rho_{T,int}}\right)\left(\frac{Al_B}{Al_{tot}}\right)\left(\frac{A_s}{V}\right)\eta^{-1} \quad (13)$$

assuming that the Si/Al ratio does not change between the surface and bulk of the zeolite, where k_{ext}/k_{int} is the ratio of effective first-order rate constants for external sites and internal Brønsted acid sites, Al_B/Al_{tot} is the fraction of external Al that forms exclusively Brønsted acid sites (and not trivalent Lewis acidic Al), η is the effectiveness factor, and $\rho_{T,ext}$ and $\rho_{T,int}$ are the densities of T-sites on the outer surface and within the bulk, respectively, and have values of 0.0894 Å^{-2} for the surface model used in this work and 0.0180 Å^{-3} for bulk MFI, respectively. From this work, we estimate an Al_B/Al_{tot} of 0.75 and a $\rho_{T,ext}/\rho_{T,int}$ of 4.967 Å, based on the studied model. The values of A_s/V and η depend on the shape of the catalyst particles. We compare two models for spherical and slab catalyst models, where A_s/V expressions are

$$\left(\frac{A_s}{V}\right)_{sphere} = \frac{4\pi R^2}{\frac{4}{3}\pi R^3} = \frac{3}{R} \quad (14)$$

$$\left(\frac{A_s}{V}\right)_{slab} = \frac{ab}{2Lab} = \frac{1}{2L} \quad (15)$$

where R is the radius of a spherical particle, L is half the thickness of the slab (in the direction along which reactants

https://doi.org/10.1021/acscatal.3c00076
ACS Catal. 2023, 13, 4470−4487

can diffuse), and a and b are the width and height of a slab, respectively. The η values are

$$\eta_{\text{sphere}} = \frac{3}{\Phi^2}(\Phi \coth \Phi - 1) \tag{16}$$

$$\eta_{\text{slab}} = \tanh \Phi/\Phi \tag{17}$$

which depend on the Thiele modulus, Φ[114]

$$\Phi = L\sqrt{\frac{k_{\text{int}}\,\rho_{\text{T,int}}\left(1 + \left(\frac{\text{Si}}{\text{Al}}\right)_{\text{int}}\right)^{-1}}{\mathcal{D}_{\text{eff}}}} \tag{18}$$

for a first-order or pseudo-first-order reaction, which depends on the particle size, acid site density, and temperature, each of which influences effective diffusivities and rate constants within the catalyst particle. The $k_{\text{int}}\,\rho_{\text{T,int}}\,(1 + (\text{Si/Al})_{\text{int}})^{-1}$ term is defined to have units of s^{-1}.

Finned, pillared, or hierarchical zeolites have been modified to decrease diffusion path lengths and have larger A_s/V ratios, while non-hierarchical materials can have large ranges of A_s/V depending on their overall crystal size, which can vary from <100 nm to ~20 μm.[60,115,116] Prior reports allow us to estimate a range of possible A_s/V values to parameterize the above model to estimate the relative influence of external Brønsted acid sites on observed reaction rates. For example, MFI crystals with an approximately spherical shape have been synthesized with an average diameter of ~17 μm.[60] If modeled as spheres, these materials have A_s/V of 3.5×10^{-5} Å^{-1}, providing an approximate lower bound for A_s/V. MFI nanocrystals can also be synthesized with approximately spherical shapes and diameters of ~200 μm.[60,116,117] In such cases, the A_s/V would approach 3×10^{-3} Å^{-1} for approximately spherical shapes. Adding fins to FER zeolites increased A_s/V by relatively modest amounts (up to a factor of 2−3 by a combination of theoretical estimates and surface area measurements),[30] and finning in MFI zeolites increased surface areas by ~40%.[29] Mesopores introduced to MFI crystals during synthesis have been reported to increase A_s/V by a factor of ~5, with a large templating agent increasing per gram external surface areas (S_{ext}) from 46.8 to 97 m^2 g^{-1} (A_s/V = 0.009−0.018 Å^{-1}) in MFI crystals of commercial provenance to 262−392 m^2 g^{-1} (A_s/V = 0.048−0.072 Å^{-1}).[51] Pillared materials are estimated to have an A_s/V of around 0.1−0.2 Å^{-1} based on reported site characterization data.[60] These higher A_s/V values lead to higher ratios of external to internal Brønsted acid sites, with such ratios increasing from 10^{-4} on a 17 μm MFI crystal to 0.033 on a 200 nm MFI crystal and to 0.16 for mesoporous MFI and reaching a maximum of 0.78 for self-pillared MFI.[60] Together, these results indicate that A_s/V varies from 10^{-5} to 0.2 Å^{-1} in MFI samples.

While these geometries significantly vary from idealized slab and spherical geometries, effectiveness factors are not very sensitive to geometry. Therefore, we compute the ratio of the external and internal rates (using slab and spherical geometries) across A_s/V ratios of 10^{-5} to 0.5 Å^{-1} and for Φ values of 10^{-1} to 10^3, which reflect mass transport limitations for bulkier molecules that limit the effectiveness of internal sites (Figure 19). Even for reactions with a relatively weak confinement effect ($k_{\text{ext}}/k_{\text{int}} \approx 10^{-1}$, such as methanol dehydration), the ratio of rates at external to internal sites barely exceeds 0.1 at the maximum reasonable A_s/V value (0.2 Å^{-1}) when transport is not a factor ($\Phi \leq 1$; $\eta > 0.93$ for both slab and sphere models; Figure 19). This finding suggests that external sites would contribute only slightly to measured rates in regimes that are not transport-limited because confinement effects diminish the role of external sites even as the ratio of external to internal sites starts to reach parity. As the sizes of key transition states approach the void sizes within the zeolite, confinement effects will increase (decreasing $k_{\text{ext}}/k_{\text{int}}$), also diminishing the role of external sites. However, the larger molecules involved in these transition states would have lower effective diffusivities, increasing Φ and the role of external sites. As reactants and transition states become larger than the void sites in MFI, external sites become more important because low diffusivities prevent reactive species from entering the bulk of the crystal. In extreme cases, reactions will only occur at external sites because of effective diffusivities approaching zero (causing $\Phi \rightarrow \infty$ and $\eta \rightarrow 0$). For example, mesitylene alkylation with benzyl alcohol has turnover rates that are invariant with external Brønsted acid site counts, and rates thus increase with A_s/V.[48,60]

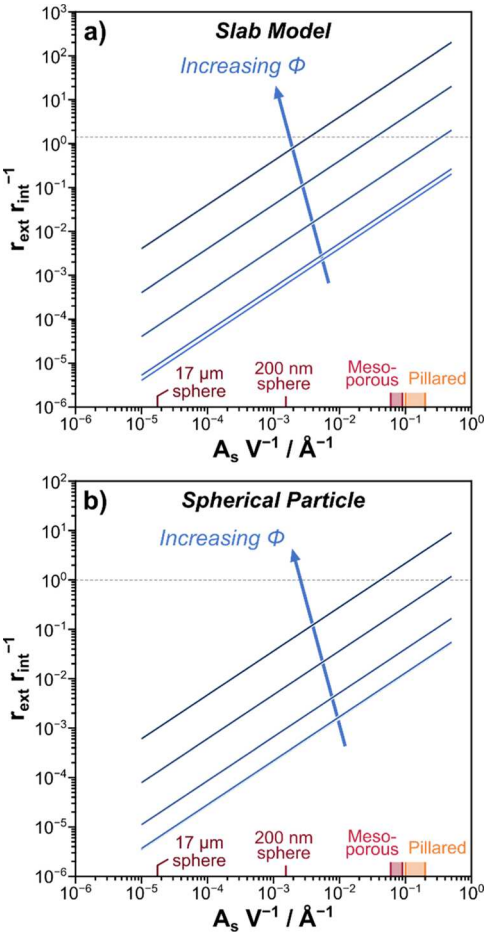

Figure 19. Ratio of rates on external sites to those on internal sites ($r_{\text{ext}}\,r_{\text{int}}^{-1}$) on (a) a slab model and (b) a spherical particle model as a function of the surface-area-to-volume ratio ($A_s\,V^{-1}$) for Thiele moduli (Φ) of 10^{-1}, 10^0, 10^1, 10^2, and 10^3. The horizontal dashed gray line indicates where the external rate contribution eclipses that of the internal rate contribution.

We believe that this analysis enables a more direct assessment of confinement effects in zeolites that accounts for the influence of external sites on turnover rates. In principle, by performing kinetic measurements for a reaction on mesoporous materials without micropores (e.g., MCM-41)

https://doi.org/10.1021/acscatal.3c00076
ACS Catal. 2023, 13, 4470−4487

and in zeolite samples with identical frameworks but varying crystal sizes or habits (and therefore A_s/V), confinement and k_{ext}/k_{int} ratios can be estimated. Analogously, DFT calculations for reactions on 2D zeolite models and on similar external surface models and bulk models could be used for similar investigations. Ultimately, such data could be used to parameterize continuum-based kinetic models or kinetic Monte Carlo (KMC)[118,119] models that rigorously predict the effects of changing crystal habits on observed rate.

4. CONCLUSIONS

We use a combination of metrics—DPE, DHE, and NH_3 BE (ΔE_{NH_3})—to compare the acid strength of all T-sites in the bulk and on the external (010) surface of MFI. Ensemble average DPE (1644−1664 kJ mol^{-1}) and DHE (457−476 kJ mol^{-1}) values linearly correlate and have ranges of 20 kJ mol^{-1} across all T-sites within the MFI bulk. This range of 20 kJ mol^{-1} is similar to that observed, in a prior work, among T-sites across a range of zeolite frameworks.[34] The similar behavior between DPE and DHE for these sites indicates that both metrics reflect EAs that do not change with different Al positions within the MFI framework. Unlike DHE, ΔE_{NH_3} values do not correlate well with DPE because this metric convolutes confinement effects in addition to the energy to heterolytically cleave the O−H bond of the Brønsted acid site. Confinement differs between Al locations depending on the local environment each T-site can access. As such, we caution against using ΔE_{NH_3}, or the adsorption of any other base, to determine Brønsted acid strength.

We identify two classes of T-sites on the MFI surface model based on their distance from the vacuum slab: internal and external sites. Internal sites retain a similar local environment to sites within the MFI bulk and are farther from the vacuum slab. External sites, on the other hand, comprise the closest layer of T-sites to the vacuum space. All dangling Si and O bonds on the surface were terminated as silanol (Si−OH) groups when cleaving the surface; as such, substituting Al into these positions (T7, T9, T10, and T12) and adding a proton to the terminal OH group yields H_2O bound to a Lewis acidic Al. We substitute Al into all 12 internal and 12 external T-site positions and use the same acid strength metrics to compare the surface model of MFI to the bulk model.

Ensemble average DPE values are much lower on the (010) surface model with 10 Å of vacuum (1477−1543 kJ mol^{-1}) than they are in the MFI bulk (1644−1664 kJ mol^{-1}). The T-site locations that produce Lewis acidic H_2O−Al complexes are the weakest acid sites, with ensemble average DPE values of 1533−1543 kJ mol^{-1}. Other external sites have similar DPE values (1486−1513 kJ mol^{-1}) to internal sites on the surface model (1477−1506 kJ mol^{-1}), which behave nearly identically to the bulk sites. This result indicates that Brønsted acid strength is not affected by the proximity of the Al to the MFI surface absent Al substitution at Si−OH sites that form Lewis acids.

Ensemble average DHE and ΔE_{NH_3} values are similar on the surface model and the bulk model. These methods do not produce any charged species in our periodic calculations and, therefore, are unhindered by the artifacts that charged calculations produce. Ensemble average DHE values for surface sites that do not form Lewis acids (457−483 kJ mol^{-1}) are very similar to their bulk counterparts (457−476 kJ mol^{-1}). Sites that form Lewis acids have DHE values that are similar to those of other surface sites (471−495 kJ mol^{-1}). These similar DHE values between exclusively Brønsted acidic Al sites and H_2O bound to Lewis acidic Al sites on the surface model show that differences in acid strength between these two site types do not necessarily arise because of strict differences in O−H bond strength. Instead, Lewis acidic Al sites stabilize anionic charge less effectively than Brønsted sites upon deprotonation of a bound H_2O molecule.

Finally, we also study the Lewis acid strength of trigonal planar Al that form in the T7, T9, T10, and T12 positions on the MFI surface. When H_2O is bound to these sites, we can calculate DPE, DHE, and NH_3 BEs similar to that of other Brønsted acid sites; however, if H_2O desorbs, NH_3 can bind directly to the Al as a Lewis base ($\Delta E_{NH_3,L}$). These $\Delta E_{NH_3,L}$ values suggest that NH_3 binds more strongly to Lewis sites (−190 to −171 kJ mol^{-1}) than all Brønsted acid sites in the bulk (ensemble average ΔE_{NH_3} of −160 to −133 kJ mol^{-1}), where adsorbates are most confined.

We estimate the effect that these external sites can have on observed reaction rates in zeolites by computing the ratio of rates at external sites to those at internal sites (r_{ext}/r_{int}). We develop a model that describes this ratio as a function of the ratio of external and internal rate constants—which only depend on confinement, based on the DPE values computed in this work—the surface-area-to-volume ratio (A_s/V), the ratio of T-site densities on the surface and in the bulk ($\rho_{T,ext}/\rho_{T,int}$), the fraction of Al positions on the surface that form only Brønsted acid sites (Al_B/Al_{tot}), and the effectiveness factor, η. This model indicates that external sites can contribute significantly to rates despite their reduced confinement. Net rates at external sites can reach up to 12% those of internal sites even with very low Φ (and high η) when A_s/V values are sufficiently high (>0.2 Å^{-1}).

Taken together, these data show that acid strength for most sites at the surfaces of zeolites are similar to those within the zeolite crystal unless they form trigonal planar Lewis acidic sites on the outside of zeolite crystals. The similarity of Brønsted acid strength between surface and internal sites in the MFI zeolite suggests that reactivity differences between such sites can be solely attributed to confinement effects. Reactions with bulky intermediates such as diphenylmethane formation[57] and Friedel−Crafts alkylation of benzene[58,59] occur at external sites only because such sites have sufficient volume for intermediates to form and not because of differences in reactivity. As such, this study provides valuable insights into contemporary reactivity studies on high-surface-area zeolites or on zeolites with zoned Al distributions to increase or decrease the prevalence of external sites.

■ ASSOCIATED CONTENT

Supporting Information

The Supporting Information is available free of charge at https://pubs.acs.org/doi/10.1021/acscatal.3c00076.

Images of H-form and NH_4-form bulk MFI structures, EAs for all sites in the bulk MFI, correlations between NH_3 BE and DHE, images of H-form and NH_4-form structures of the internal and external sites of the MFI surface model, dependence of DPE on the vacuum spacing in the surface model, and derivation of the relative rates on external and internal sites (PDF)

https://doi.org/10.1021/acscatal.3c00076
ACS Catal. 2023, 13, 4470−4487

AUTHOR INFORMATION

Corresponding Author

David Hibbitts − *Department of Chemical Engineering, University of Florida, Gainesville, Florida 32611, United States;* orcid.org/0000-0001-8606-7000; Email: hibbitts@che.ufl.edu

Authors

Haliey Balcom − *Department of Chemical Engineering, University of Florida, Gainesville, Florida 32611, United States*

Alexander J. Hoffman − *Department of Chemical Engineering, University of Florida, Gainesville, Florida 32611, United States;* Present Address: Massachusetts Institute of Technology, Cambridge, MA 02139, USA; orcid.org/0000-0002-1337-9297

Huston Locht − *Department of Chemical Engineering, University of Florida, Gainesville, Florida 32611, United States;* Present Address: University of Illinois at Urbana-Champaign, Urbana, IL 61801, USA.

Complete contact information is available at: https://pubs.acs.org/10.1021/acscatal.3c00076

Author Contributions

[§]H.B. and A.J.H. contributed equally.

Notes

The authors declare no competing financial interest.

ACKNOWLEDGMENTS

This work was supported by the National Science Foundation CAREER program under award 1942684-CBET. This work used the Extreme Science and Engineering Discovery Environment (XSEDE),[120] which is supported by the National Science Foundation grant number ACI-1548562 through allocation CTS160041. Additional computational resources were provided by the University of Florida Research Computing. The authors also thank Nikki Kragt for careful proofreading of the manuscript.

REFERENCES

(1) Vermeiren, W.; Gilson, J. P. Impact of zeolites on the petroleum and petrochemical industry. *Top. Catal.* **2009**, *52*, 1131−1161.

(2) Corma, A. From microporous to mesoporous molecular sieve materials and their use in catalysis. *Chem. Rev.* **1997**, *97*, 2373−2420.

(3) Corma, A. Inorganic Solid Acids and Their Use in Acid-Catalyzed Hydrocarbon Reactions. *Chem. Rev.* **1995**, *95*, 559−614.

(4) Derouane, E. A novel effect of shape selectivity: Molecular traffic control in zeolite ZSM-5. *J. Catal.* **1980**, *65*, 486−489.

(5) Csicsery, S. M. Shape-selective catalysis in zeolites. *Zeolites* **1984**, *4*, 202−213.

(6) Chen, N. Y.; Kaeding, W. W.; Dwyer, F. G. Para-directed aromatic reactions over shape-selective molecular sieve zeolite catalysts. *J. Am. Chem. Soc.* **1979**, *101*, 6783−6784.

(7) Hill, I.; Malek, A.; Bhan, A. Kinetics and Mechanism of Benzene, Toluene, and Xylene Methylation over H-MFI. *ACS Catal.* **2013**, *3*, 1992−2001.

(8) DeLuca, M.; Kravchenko, P.; Hoffman, A.; Hibbitts, D. Mechanism and Kinetics of Methylating C_6 −C_{12} Methylbenzenes with Methanol and Dimethyl Ether in H-MFI Zeolites. *ACS Catal.* **2019**, *9*, 6444−6460.

(9) Gounder, R.; Iglesia, E. Effects of partial confinement on the specificity of monomolecular alkane reactions for acid sites in side pockets of mordenite. *Angew. Chem., Int. Ed.* **2010**, *49*, 808−811.

(10) Gounder, R.; Iglesia, E. Catalytic consequences of spatial constraints and acid site location for monomolecular alkane activation on zeolites. *J. Am. Chem. Soc.* **2009**, *131*, 1958−1971.

(11) Olsbye, U.; Svelle, S.; Bjørgen, M.; Beato, P.; Janssens, T. V. W.; Joensen, F.; Bordiga, S.; Lillerud, K. P. Conversion of methanol to hydrocarbons: how zeolite cavity and pore size controls product selectivity. *Angew. Chem., Int. Ed.* **2012**, *51*, 5810−5831.

(12) Kang, J. H.; Alshafei, F. H.; Zones, S. I.; Davis, M. E. Cage-Defining Ring: A Molecular Sieve Structural Indicator for Light Olefin Product Distribution from the Methanol-to-Olefins Reaction. *ACS Catal.* **2019**, *9*, 6012−6019.

(13) Ferri, P.; Li, C.; Millán, R.; Martínez-Triguero, J.; Moliner, M.; Boronat, M.; Corma, A. Impact of Zeolite Framework Composition and Flexibility on Methanol-To-Olefins Selectivity: Confinement or Diffusion? *Angew. Chem., Int. Ed.* **2020**, *59*, 19708−19715.

(14) Li, J.; Wei, Y.; Chen, J.; Xu, S.; Tian, P.; Yang, X.; Li, B.; Wang, J.; Liu, Z. Cavity controls the selectivity: insights of confinement effects on MTO reaction. *ACS Catal.* **2015**, *5*, 661−665.

(15) Kang, J. H.; Walter, R.; Xie, D.; Davis, T.; Chen, C.-Y.; Davis, M. E.; Zones, S. I. Further studies on how the nature of zeolite cavities that are bounded by small pores influences the conversion of methanol to light olefins. *ChemPhysChem* **2018**, *19*, 412−419.

(16) Bhawe, Y.; Moliner-Marin, M.; Lunn, J. D.; Liu, Y.; Malek, A.; Davis, M. Effect of cage size on the selective conversion of methanol to light olefins. *ACS Catal.* **2012**, *2*, 2490−2495.

(17) Sarazen, M. L.; Doskocil, E.; Iglesia, E. Effects of void environment and acid strength on alkene oligomerization selectivity. *ACS Catal.* **2016**, *6*, 7059−7070.

(18) Allen, M. C.; Hoffman, A. J.; Liu, T.; Webber, M. S.; Hibbitts, D.; Schwartz, T. J. Highly Selective Cross-Etherification of 5-Hydroxymethylfurfural with Ethanol. *ACS Catal.* **2020**, *10*, 6771−6785.

(19) Jae, J.; Tompsett, G. A.; Foster, A. J.; Hammond, K. D.; Auerbach, S. M.; Lobo, R. F.; Huber, G. W. Investigation into the shape selectivity of zeolite catalysts for biomass conversion. *J. Catal.* **2011**, *279*, 257−268.

(20) Yu, Y.; Li, X.; Su, L.; Zhang, Y.; Wang, Y.; Zhang, H. The role of shape selectivity in catalytic fast pyrolysis of lignin with zeolite catalysts. *Appl. Catal., A* **2012**, *447*−*448*, 115−123.

(21) Jones, A. J.; Zones, S. I.; Iglesia, E. Implications of Transition State Confinement within Small Voids for Acid Catalysis. *J. Phys. Chem. C* **2014**, *118*, 17787−17800.

(22) Carr, R. T.; Neurock, M.; Iglesia, E. Catalytic consequences of acid strength in the conversion of methanol to dimethyl ether. *J. Catal.* **2011**, *278*, 78−93.

(23) Sarazen, M. L.; Doskocil, E.; Iglesia, E. Catalysis on solid acids: Mechanism and catalyst descriptors in oligomerization reactions of light alkenes. *J. Catal.* **2016**, *344*, 553−569.

(24) Pérez-Ramírez, J.; Christensen, C. H.; Egeblad, K.; Christensen, C. H.; Groen, J. C. Hierarchical zeolites: enhanced utilisation of microporous crystals in catalysis by advances in materials design. *Chem. Soc. Rev.* **2008**, *37*, 2530−2542.

(25) Tao, Y.; Kanoh, H.; Abrams, L.; Kaneko, K. Mesopore-modified zeolites: preparation, characterization, and applications. *Chem. Rev.* **2006**, *106*, 896−910.

(26) Schulman, E.; Wu, W.; Liu, D. Two-Dimensional Zeolite Materials: Structural and Acidity Properties. *materials* **2020**, *13*, 1822.

(27) He, Y. J.; Nivarthy, G. S.; Eder, F.; Seshan, K.; Lercher, J. A. Synthesis, characterization and catalytic activity of the pillared molecular sieve MCM-36. *Microporous Mesoporous Mater.* **1998**, *25*, 207−224.

(28) Na, K.; Choi, M.; Park, W.; Sakamoto, Y.; Terasaki, O.; Ryoo, R. Pillared MFI zeolite nanosheets of a single-unit-cell thickness. *J. Am. Chem. Soc.* **2010**, *132*, 4169−4177.

(29) Dai, H.; Shen, Y.; Yang, T.; Lee, C.; Fu, D.; Agarwal, A.; Le, T. T.; Tsapatsis, M.; Palmer, J. C.; Weckhuysen, B. M.; Dauenhauer, P. J.; Zou, X.; Rimer, J. D. Finned zeolite catalysts. *Nat. Mater.* **2020**, *19*, 1074−1080.

(30) Dai, H.; Lee, C.; Liu, W.; Yang, T.; Claret, J.; Zou, X.; Dauenhauer, P. J.; Li, X.; Rimer, J. D. Enhanced selectivity and stability of finned ferrierite catalysts in butene isomerization. *Angew. Chem., Int. Ed.* **2022**, *61*, No. e202113077.
(31) Jones, A. J.; Carr, R. T.; Zones, S. I.; Iglesia, E. Acid strength and solvation in catalysis by MFI zeolites and effects of the identity, concentration and location of framework heteroatoms. *J. Catal.* **2014**, *312*, 58−68.
(32) Chatterjee, A.; Iwasaki, T.; Ebina, T.; Miyamoto, A. Density functional study for estimating Brønsted acid site strength in isomorphously substituted ZSM-5. *Microporous Mesoporous Mater.* **1998**, *21*, 421−428.
(33) Yuan, S. P.; Wang, J. G.; Li, Y. W.; Jiao, H. Brønsted Acidity of Isomorphously Substituted ZSM-5 by B, Al, Ga, and Fe. Density Functional Investigations. *J. Phys. Chem. A* **2002**, *106*, 8167−8172.
(34) Jones, A. J.; Iglesia, E. The strength of Brønsted acid sites in microporous aluminosilicates. *ACS Catal.* **2015**, *5*, 5741−5755.
(35) Rybicki, M.; Sauer, J. Acid strength of zeolitic Brønsted sites — dependence on dielectric properties. *Catal. Today* **2019**, *323*, 86−93.
(36) Nystrom, S.; Hoffman, A.; Hibbitts, D. Tuning Brønsted acid strength by altering site proximity in CHA framework zeolites. *ACS Catal.* **2018**, *8*, 7842−7860.
(37) Katada, N.; Suzuki, K.; Noda, T.; Sastre, G.; Niwa, M. Correlation between Brønsted Acid Strength and Local Structure in Zeolites. *J. Phys. Chem. C* **2009**, *113*, 19208−19217.
(38) Suzuki, K.; Noda, T.; Katada, N.; Niwa, M. IRMS-TPD of ammonia: Direct and individual measurement of Brønsted acidity in zeolites and its relationship with the catalytic cracking activity. *J. Catal.* **2007**, *250*, 151−160.
(39) Liu, C.; Li, G.; Hensen, E. J. M.; Pidko, E. A. Relationship between acidity and catalytic reactivity of faujasite zeolite: A periodic DFT study. *J. Catal.* **2016**, *344*, 570−577.
(40) Liu, C.; Tranca, I.; van Santen, R. A.; Hensen, E. J. M.; Pidko, E. A. Scaling relations for acidity and reactivity of zeolites. *J. Phys. Chem. C Nanomater. Interfaces* **2017**, *121*, 23520−23530.
(41) Parrillo, D. J.; Gorte, R. J. Characterization of acidity in H-ZSM-5, H-ZSM-12, H-Mordenite, and H-Y using microcalorimetry. *J. Phys. Chem.* **1993**, *97*, 8786−8792.
(42) Lee, C.; Parrillo, D. J.; Gorte, R. J.; Farneth, W. E. Relationship between Differential Heats of Adsorption and Brønsted Acid Strengths of Acidic Zeolites: H-ZSM-5 and H-Mordenite. *J. Am. Chem. Soc.* **1996**, *118*, 3262−3268.
(43) Gorte, R. J.; Crossley, S. P. A perspective on catalysis in solid acids. *J. Catal.* **2019**, *375*, 524−530.
(44) Demmin, R.; Gorte, R. J. Design parameters for temperature-programmed desorption from a packed bed. *J. Catal.* **1984**, *90*, 32−39.
(45) Gorte, R. Design parameters for temperature programmed desorption from porous catalysts. *J. Catal.* **1982**, *75*, 164−174.
(46) Gorte, R. J. What do we know about the acidity of solid acids? *Catal. Lett.* **1999**, *62*, 1−13.
(47) Hibbitts, D.; Tan, Q.; Neurock, M. Acid strength and bifunctional catalytic behavior of alloys comprised of noble metals and oxophilic metal promoters. *J. Catal.* **2014**, *315*, 48−58.
(48) Zhang, X.; Liu, D.; Xu, D.; Asahina, S.; Cychosz, K. A.; Agrawal, K. V.; Al Wahedi, Y.; Bhan, A.; Al Hashimi, S.; Terasaki, O.; Thommes, M.; Tsapatsis, M. Synthesis of self-pillared zeolite nanosheets by repetitive branching. *Science* **2012**, *336*, 1684−1687.
(49) Ma, Y.; Tang, X.; Hu, J.; Ma, Y.; Chen, W.; Liu, Z.; Han, S.; Xu, C.; Wu, Q.; Zheng, A.; Zhu, L.; Meng, X.; Xiao, F.-S. Design of a Small Organic Template for the Synthesis of Self-Pillared Pentasil Zeolite Nanosheets. *J. Am. Chem. Soc.* **2022**, *144*, 6270−6277.
(50) Wei, L.; Song, K.; Wu, W.; Holdren, S.; Zhu, G.; Shulman, E.; Shang, W.; Chen, H.; Zachariah, M. R.; Liu, D. Vapor-Phase Strategy to Pillaring of Two-Dimensional Zeolite. *J. Am. Chem. Soc.* **2019**, *141*, 8712−8716.
(51) Choi, M.; Na, K.; Kim, J.; Sakamoto, Y.; Terasaki, O.; Ryoo, R. Stable single-unit-cell nanosheets of zeolite MFI as active and long-lived catalysts. *Nature* **2009**, *461*, 246−249.
(52) Jeon, M. Y.; Kim, D.; Kumar, P.; Lee, P. S.; Rangnekar, N.; Bai, P.; Shete, M.; Elyassi, B.; Lee, H. S.; Narasimharao, K.; Basahel, S. N.; Al-Thabaiti, S.; Xu, W.; Cho, H. J.; Fetisov, E. O.; Thyagarajan, R.; DeJaco, R. F.; Fan, W.; Mkhoyan, K. A.; Siepmann, J. I.; Tsapatsis, M. Ultra-selective high-flux membranes from directly synthesized zeolite nanosheets. *Nature* **2017**, *543*, 690−694.
(53) Roth, W. J.; Kresge, C. T.; Vartuli, J. C.; Leonowicz, M. E.; Fung, A. S.; McCullen, S. B. MCM-36: The first pillared molecular sieve with zeoliteproperties. In *Catalysis by Microporous Materials, Proceedings of ZEOCAT '95*; *Studies in Surface Science and Catalysis*; Elsevier, 1995; Vol. *94*, pp 301−308.
(54) Khare, R.; Bhan, A. Mechanistic studies of methanol-to-hydrocarbons conversion on diffusion-free MFI samples. *J. Catal.* **2015**, *329*, 218−228.
(55) Le, T. T.; Shilpa, K.; Lee, C.; Han, S.; Weiland, C.; Bare, S. R.; Dauenhauer, P. J.; Rimer, J. D. Core-shell and Egg-shell Zeolite Catalysts for Enhanced Hydrocarbon Processing. *J. Catal.* **2022**, *405*, 664.
(56) Le, T. T.; Chawla, A.; Rimer, J. D. Impact of acid site speciation and spatial gradients on zeolite catalysis. *J. Catal.* **2020**, *391*, 56−68.
(57) Foley, B. L.; Bhan, A. Transient and Steady-State Kinetic Studies of Formaldehyde Alkylation of Benzene to Form Diphenylmethane on HZSM-5 Catalysts. *ACS Catal.* **2020**, *10*, 10436−10448.
(58) Li, X.; Prins, R.; van Bokhoven, J. A. Synthesis and characterization of mesoporous mordenite. *J. Catal.* **2009**, *262*, 257−265.
(59) Sun, Y.; Prins, R. Friedel-Crafts alkylations over hierarchical zeolite catalysts. *Appl. Catal., A* **2008**, *336*, 11−16.
(60) Liu, D.; Zhang, X.; Bhan, A.; Tsapatsis, M. Activity and selectivity differences of external Brønsted acid sites of single-unit-cell thick and conventional MFI and MWW zeolites. *Microporous Mesoporous Mater.* **2014**, *200*, 287−290.
(61) Adawi, H. I.; Odigie, F. O.; Sarazen, M. L. Alkylation of poly-substituted aromatics to probe effects of mesopores in hierarchical zeolites with differing frameworks and crystal sizes. *Mol. Syst. Des. Eng.* **2021**, *6*, 903−917.
(62) Emdadi, L.; Oh, S. C.; Wu, Y.; Oliaee, S. N.; Diao, Y.; Zhu, G.; Liu, D. The role of external acidity of meso-/microporous zeolites in determining selectivity for acid-catalyzed reactions of benzyl alcohol. *J. Catal.* **2016**, *335*, 165−174.
(63) Wu, Y.; Emdadi, L.; Qin, D.; Zhang, J.; Liu, D. Quantification of external surface and pore mouth acid sites in unit-cell thick pillared MFI and pillared MWW zeolites. *Microporous Mesoporous Mater.* **2017**, *241*, 43−51.
(64) Liu, D.; Bhan, A.; Tsapatsis, M.; Al Hashimi, S. Catalytic Behavior of Brønsted Acid Sites in MWW and MFI Zeolites with Dual Meso- and Microporosity. *ACS Catal.* **2011**, *1*, 7−17.
(65) Treps, L.; Gomez, A.; de Bruin, T.; Chizallet, C. Environment, Stability and Acidity of External Surface Sites of Silicalite-1 and ZSM-5 Micro and Nano Slabs, Sheets, and Crystals. *ACS Catal.* **2020**, *10*, 3297−3312.
(66) Rey, J.; Raybaud, P.; Chizallet, C. Ab initio simulation of the acid sites at the external surface of zeolite beta. *ChemCatChem* **2017**, *9*, 2176−2185.
(67) Díaz, I.; Kokkoli, E.; Terasaki, O.; Tsapatsis, M. Surface structure of zeolite (MFI) crystals. *Chem. Mater.* **2004**, *16*, 5226−5232.
(68) Chizallet, C. Toward the atomic scale simulation of intricate acidic aluminosilicate catalysts. *ACS Catal.* **2020**, *10*, 5579−5601.
(69) Roeffaers, M. B. J.; Ameloot, R.; Baruah, M.; Uji-i, H.; Bulut, M.; De Cremer, G.; Müller, U.; Jacobs, P. A.; Hofkens, J.; Sels, B. F.; De Vos, D. E. Morphology of large ZSM-5 crystals unraveled by fluorescence microscopy. *J. Am. Chem. Soc.* **2008**, *130*, 5763−5772.
(70) Bukowski, B. C.; Bates, J. S.; Gounder, R.; Greeley, J. Defect-Mediated Ordering of Condensed Water Structures in Microporous Zeolites. *Angew. Chem., Int. Ed.* **2019**, *58*, 16422−16426.
(71) Bates, J. S.; Bukowski, B. C.; Harris, J. W.; Greeley, J.; Gounder, R. Distinct Catalytic Reactivity of Sn Substituted in Framework

Locations and at Defect Grain Boundaries in Sn-Zeolites. *ACS Catal.* **2019**, *9*, 6146−6168.
(72) Vayssilov, G. N.; Aleksandrov, H. A.; Dib, E.; Costa, I. M.; Nesterenko, N.; Mintova, S. Superacidity and spectral signatures of hydroxyl groups in zeolites. *Microporous Mesoporous Mater.* **2022**, *343*, 112144.
(73) Huber, P.; Studt, F.; Plessow, P. N. Reactivity of Surface Lewis and Brønsted Acid Sites in Zeolite Catalysis: A Computational Case Study of DME Synthesis Using H-SSZ-13. *J. Phys. Chem. C* **2022**, *126*, 5896−5905.
(74) Kresse, G.; Hafner, J. Ab initio molecular dynamics for liquid metals. *Phys. Rev. B: Condens. Matter Mater. Phys.* **1993**, *47*, 558−561.
(75) Kresse, G.; Furthmüller, J. Efficiency of ab-initio total energy calculations for metals and semiconductors using a plane-wave basis set. *Comput. Mater. Sci.* **1996**, *6*, 15−50.
(76) Kresse, G.; Furthmüller, J. Efficient iterative schemes for ab initio total-energy calculations using a plane-wave basis set. *Phys. Rev. B: Condens. Matter Mater. Phys.* **1996**, *54*, 11169−11186.
(77) Kresse, G.; Hafner, J. Ab initio molecular-dynamics simulation of the liquid-metal−amorphous-semiconductor transition in germanium. *Phys. Rev. B: Condens. Matter Mater. Phys.* **1994**, *49*, 14251−14269.
(78) Kravchenko, P.; Plaisance, C.; Hibbitts, D. A new computational interface for catalysis, 2019, Published as pre-print on. https://chemrxiv.org/articles/preprint/8040737.
(79) Perdew, J. P.; Burke, K.; Ernzerhof, M. Generalized gradient approximation made simple. *Phys. Rev. Lett.* **1996**, *77*, 3865−3868.
(80) Grimme, S. Semiempirical GGA-type density functional constructed with a long-range dispersion correction. *J. Comput. Chem.* **2006**, *27*, 1787−1799.
(81) Grimme, S.; Ehrlich, S.; Goerigk, L. Effect of the damping function in dispersion corrected density functional theory. *J. Comput. Chem.* **2011**, *32*, 1456−1465.
(82) Goncalves, T. J.; Plessow, P. N.; Studt, F. On the accuracy of density functional theory in zeolite catalysis. *ChemCatChem* **2019**, *11*, 4368−4376.
(83) Plessow, P. N.; Studt, F. How accurately do approximate density functionals predict trends in acidic zeolite catalysis? *J. Phys. Chem. Lett.* **2020**, *11*, 4305−4310.
(84) Kresse, G.; Joubert, D. From ultrasoft pseudopotentials to the projector augmented-wave method. *Phys. Rev. B: Condens. Matter Mater. Phys.* **1999**, *59*, 1758−1775.
(85) Blöchl, P. E. Projector augmented-wave method. *Phys. Rev. B: Condens. Matter Mater. Phys.* **1994**, *50*, 17953−17979.
(86) Van Koningsveld, H. High-temperature (350 K) orthorhombic framework structure of zeolite H-ZSM-5. *Acta Crystallogr., Sect. B: Struct. Sci.* **1990**, *46*, 731−735.
(87) Baerlocher, C.; McCusker, L. B. Database of Zeolite Structures. http://www.iza-structure.org/databases/ (accessed Oct 9, 2019).
(88) Baerlocher, C.; McCusker, L. B.; Olson, D. H. *Atlas of Zeolite Framework Types*, 6th ed.; Elsevier, 2007.
(89) Hoffman, A.; DeLuca, M.; Hibbitts, D. Restructuring of MFI framework zeolite models and their associated artifacts in density functional theory calculations. *J. Phys. Chem. C* **2019**, *123*, 6572−6585.
(90) Janik, M. J.; Davis, R. J.; Neurock, M. Anhydrous and water-assisted proton mobility in phosphotungstic acid. *J. Am. Chem. Soc.* **2005**, *127*, 5238−5245.
(91) Liu, P.; Mei, D. Identifying Free Energy Landscapes of Proton-Transfer Processes between Brønsted Acid Sites and Water Clusters Inside the Zeolite Pores. *J. Phys. Chem. C* **2020**, *124*, 22568−22576.
(92) Ryder, J. A.; Chakraborty, A. K.; Bell, A. T. Density Functional Theory Study of Proton Mobility in Zeolites: Proton Migration and Hydrogen Exchange in ZSM-5. *J. Phys. Chem. B* **2000**, *104*, 6998−7011.
(93) Di Iorio, J. R.; Hoffman, A. J.; Nimlos, C. T.; Nystrom, S.; Hibbitts, D.; Gounder, R. Mechanistic origins of the high-pressure inhibition of methanol dehydration rates in small-pore acidic zeolites. *J. Catal.* **2019**, *380*, 161−177.
(94) Di Iorio, J. R.; Nimlos, C. T.; Gounder, R. Introducing Catalytic Diversity into Single-Site Chabazite Zeolites of Fixed Composition via Synthetic Control of Active Site Proximity. *ACS Catal.* **2017**, *7*, 6663−6674.
(95) Hoffman, A. J.; Bates, J. S.; Di Iorio, J. R.; Nystrom, S. V.; Nimlos, C. T.; Gounder, R.; Hibbitts, D. Rigid arrangements of ionic charge in zeolite frameworks conferred by specific aluminum distributions preferentially stabilize alkanol dehydration transition states. *Angew. Chem., Int. Ed.* **2020**, *59*, 18686−18694.
(96) Ravi, M.; Sushkevich, V. L.; van Bokhoven, J. A. Towards a better understanding of Lewis acidic aluminium in zeolites. *Nat. Mater.* **2020**, *19*, 1047−1056.
(97) Nimlos, C. T.; Hoffman, A. J.; Hur, Y. G.; Lee, B. J.; Di Iorio, J. R.; Hibbitts, D. D.; Gounder, R. Experimental and Theoretical Assessments of Aluminum Proximity in MFI Zeolites and Its Alteration by Organic and Inorganic Structure-Directing Agents. *Chem. Mater.* **2020**, *32*, 9277−9298.
(98) Fletcher, R. E.; Ling, S.; Slater, B. Violations of Löwenstein's rule in zeolites. *Chem. Sci.* **2017**, *8*, 7483−7491.
(99) Tang, X.; Liu, Z.; Huang, L.; Chen, W.; Li, C.; Wang, G.; Li, G.; Yi, X.; Zheng, A. Violation or abidance of Löwenstein's rule in zeolites under synthesis conditions? *ACS Catal.* **2019**, *9*, 10618−10625.
(100) Di Iorio, J. R.; Li, S.; Jones, C. B.; Nimlos, C. T.; Wang, Y.; Kunkes, E.; Vattipalli, V.; Prasad, S.; Moini, A.; Schneider, W. F.; Gounder, R. Cooperative and Competitive Occlusion of Organic and Inorganic Structure-Directing Agents within Chabazite Zeolites Influences Their Aluminum Arrangement. *J. Am. Chem. Soc.* **2020**, *142*, 4807−4819.
(101) Li, S.; Li, H.; Gounder, R.; Debellis, A.; Müller, I. B.; Prasad, S.; Moini, A.; Schneider, W. F. First-Principles Comparison of Proton and Divalent Copper Cation Exchange Energy Landscapes in SSZ-13 Zeolite. *J. Phys. Chem. C* **2018**, *122*, 23564−23573.
(102) Knaeble, W.; Iglesia, E. Acid strength and metal-acid proximity effects on methylcyclohexane ring contraction turnover rates and selectivities. *J. Catal.* **2016**, *344*, 817−830.
(103) Knaeble, W.; Carr, R. T.; Iglesia, E. Mechanistic interpretation of the effects of acid strength on alkane isomerization turnover rates and selectivity. *J. Catal.* **2014**, *319*, 283−296.
(104) Noh, G.; Zones, S. I.; Iglesia, E. Consequences of Acid Strength and Diffusional Constraints for Alkane Isomerization and β-Scission Turnover Rates and Selectivities on Bifunctional Metal-Acid Catalysts. *J. Phys. Chem. C* **2018**, *122*, 25475−25497.
(105) Shi, Z.; Neurock, M.; Bhan, A. Methanol-to-Olefins Catalysis on HSSZ-13 and HSAPO-34 and Its Relationship to Acid Strength. *ACS Catal.* **2021**, *11*, 1222−1232.
(106) Deshlahra, P.; Iglesia, E. Reactivity descriptors in acid catalysis: acid strength, proton affinity and host−guest interactions. *Chem. Commun.* **2020**, *56*, 7371−7398.
(107) Deshlahra, P.; Iglesia, E. Toward more complete descriptors of reactivity in catalysis by solid acids. *ACS Catal.* **2016**, *6*, 5386−5392.
(108) Deshlahra, P.; Carr, R. T.; Iglesia, E. Ionic and covalent stabilization of intermediates and transition states in catalysis by solid acids. *J. Am. Chem. Soc.* **2014**, *136*, 15229−15247.
(109) Bhan, A.; Allian, A. D.; Sunley, G. J.; Law, D. J.; Iglesia, E. Specificity of sites within eight-membered ring zeolite channels for carbonylation of methyls to acetyls. *J. Am. Chem. Soc.* **2007**, *129*, 4919−4924.
(110) Boronat, M.; Martínez-Sánchez, C.; Law, D.; Corma, A. Enzyme-like specificity in zeolites: a unique site position in mordenite for selective carbonylation of methanol and dimethyl ether with CO. *J. Am. Chem. Soc.* **2008**, *130*, 16316−16323.
(111) Cheung, P.; Bhan, A.; Sunley, G. J.; Iglesia, E. Selective carbonylation of dimethyl ether to methyl acetate catalyzed by acidic zeolites. *Angew. Chem., Int. Ed.* **2006**, *45*, 1617−1620.
(112) Bukowski, B. C.; Greeley, J. Scaling relationships for molecular adsorption and dissociation in lewis acid zeolites. *J. Phys. Chem. C* **2016**, *120*, 6714−6722.
(113) Herrmann, S.; Iglesia, E. Selective conversion of acetone to isobutene and acetic acid on aluminosilicates: Kinetic coupling

https://doi.org/10.1021/acscatal.3c00076
ACS Catal. 2023, 13, 4470−4487

between acid-catalyzed and radical-mediated pathways. *J. Catal.* **2018**, *360*, 66−80.
(114) Fogler, H. S. *Elements of Chemical Reaction Engineering*, 5th ed.; Pearson: Boston, 2016; p 957.
(115) Rimer, J. D.; Chawla, A.; Le, T. T. Crystal engineering for catalysis. *Annu. Rev. Chem. Biomol. Eng.* **2018**, *9*, 283−309.
(116) Přech, J.; Pizarro, P.; Serrano, D. P.; Čejka, J. From 3D to 2D zeolite catalytic materials. *Chem. Soc. Rev.* **2018**, *47*, 8263−8306.
(117) Mintova, S.; Grand, J.; Valtchev, V. Nanosized zeolites: Quo Vadis? *C. R. Chim.* **2016**, *19*, 183−191.
(118) Hoffmann, M. J.; Matera, S.; Reuter, K. A lattice kinetic Monte Carlo framework. *Comput. Phys. Commun.* **2014**, *185*, 2138−2150.
(119) Deluca, M.; Hibbitts, D. D. Prediction of C6−C12 Interconversion Rates Using Novel Zeolite-specific Kinetic Monte Carlo Simulation Methods. Submitted, 2020. Published as pre-print on https://chemrxiv.org/articles/preprint/8035565.
(120) Towns, J.; Cockerill, T.; Dahan, M.; Foster, I.; Gaither, K.; Grimshaw, A.; Hazlewood, V.; Lathrop, S.; Lifka, D.; Peterson, G. D.; Roskies, R.; Scott, J. R.; Wilkins-Diehr, N. XSEDE: accelerating scientific discovery. *Comput. Sci. Eng.* **2014**, *16*, 62−74.

https://doi.org/10.1021/acscatal.3c00076
ACS Catal. 2023, 13, 4470−4487